



# Thermocapillary Patterning of Highly Uniform Microarrays by Resonant Wavelength Excitation

Yi Hua Chang  and Sandra M. Troian\*

*T. J. Watson Sr. Laboratories of Applied Physics, California Institute of Technology, MC 128-95, Pasadena, California 91125, USA*

 (Received 25 June 2022; revised 8 October 2022; accepted 16 November 2022; published 29 December 2022)

For decades, researchers have been exploring pattern-forming instabilities in free surface thin films in the hope of developing alternative lithographic techniques for applications only requiring resolution limits in the submicron range. Previous studies have shown how the pitch and shape of elements in an array can be varied by adjusting the magnitude of surface forces and growth time prior to solidification *in situ*. Since the formations emerge naturally from an initial flat molten film, the final arrays exhibit ultrasoft interfaces and are therefore ideally suited to beam-shaping applications such as thin-film micro-optics. Progress in this field has stalled, however, due to the very nature of the formation process. Even when great care is taken to ensure that initial films are defect-free, final arrays still exhibit unacceptable variability in pitch, shape, and height due to ubiquitous sources of noise responsible for instability and growth. In this work, we focus on a thermocapillary instability in slender molten films exposed to a very large thermal gradient. We begin with a discussion and demonstration of why this instability inextricably leads to highly disordered arrays even if initialized by a film with very small amplitude surface roughness. We then demonstrate how spatially periodic modulation of the thermal field, implemented in three different ways, can induce synchronous growth of highly uniform periodic arrays despite noisy initial conditions. Results based on linear and weakly nonlinear stability analysis, Bloch wave analysis, and direct numerical simulation of the interface equation reveal how resonant wavelength excitations occurring between the modulation and instability driving fields are responsible for such rapid and coherent growth. An additional benefit is that the modulation field can be selected to yield an array pitch much smaller than in unmodulated systems.

DOI: [10.1103/PhysRevApplied.18.064090](https://doi.org/10.1103/PhysRevApplied.18.064090)

## I. INTRODUCTION

The field of thin-film micro-optics continues to grow rapidly, spurred by advances in thin-film technology coupled with unconventional lithographic techniques. Of special interest are thin and flexible patterned films for spatiotemporal beam shaping that can be easily integrated into small devices requiring no more than micron or sub-micron resolution. Free space micro-optical systems rely heavily on microlenslike films whose elements consist of refractive, reflective, diffractive, compound, or hybrid elements [1–4]. While some arrays are fabricated exclusively from hard material such as silicon or semiconductors, many are also being fabricated from polymeric films, which are easy to process and offer mechanical flexibility and compliancy. Polymeric films have demonstrated excellent optical performance in image focusing and magnification, image relay, collimation, filtering, low dispersion, and multispectral capability. It is anticipated that similarly patterned planar, curved, and three-dimensional

(3D) thin-film arrays will also prove useful to microfluidic, biomimetic, and metamaterial devices and sensors given they can be assembled into compact structures involving coherent coupling of multiple optical channels.

### A. Motivation

In recent years, researchers have been investigating the possibility of fabricating micro-optical arrays by contact-free lithographic techniques that rely on hydrodynamic instabilities in ultrathin polymer films [5–8]. For sufficiently large driving fields, such instabilities can be made to generate 3D periodic formations with small or large aspect ratios. Detailed knowledge of the physical mechanism leading to instability allows the user to tune the pitch (i.e., feature or element separation distance) and peak height of the patterned arrays. The three thin-film instabilities that have garnered the most attention in this regard arise from the competition between capillary forces and either thermocapillary, electrohydrodynamic, or van der Waals forces. Once the desired periodic formations are attained, the molten films are solidified

\*Corresponding author: [stroian@caltech.edu](mailto:stroian@caltech.edu)

rapidly *in situ* by dropping the temperature of the supporting substrate (typically silicon, quartz, or sapphire) below the polymer glass transition temperature. A significant advantage in using such methods to pattern films is that the final structures exhibit ultrasmooth interfaces because they are formed directly from a melt. By contrast, films patterned by conventional photolithographic methods tend to exhibit roughened interfaces due to aggressive etching processes required for delineating pattern shapes.

Early studies devoted to exploring hydrodynamic instabilities for lithographic purposes focused on the fact that films whose thickness ranges from tens of nanometers to several microns exhibit very large surface-to-volume ratios. As a result, it was anticipated that utilization of very large surface forces could provide an especially effective means by which to corral fluid initially distributed in two dimensions into three-dimensional shapes. Polymer melts of poly(methyl methacrylate), polystyrene, and polycarbonate were found to be especially amenable to such patterning methods while offering excellent optical performance. Since the surface tension of molten polymeric films is relatively small, capillary leveling is more easily overcome in such systems, allowing formation of even complex 3D liquid shapes.

Despite the enormous potential for design and fabrication of thin-film arrays by such unconventional processes, the field has stalled because of persistent problems with unacceptable variation in array pitch, shape, and height—especially problematic for optical devices that tend to have rather stringent requirements. Ironically, the very source responsible for such pattern-forming fluid instabilities—namely, ambient noise—is also responsible for the actual failure of this approach. As discussed in Sec. II, the surface forces responsible for self-organization of fluid spontaneously give rise to a runaway mechanism whereby relatively thicker regions of the film grow ever more rapidly than thinner regions. Therefore, even very small variations in initial film thickness grow rapidly to generate significant nonuniformity in pitch, shape, and height. Despite the seeming elegance of an approach that relies on a fluid instability to generate large area patterning, ubiquitous sources of noise ultimately cause nonuniformities that persist and amplify in time. It is therefore not possible to fabricate highly uniform periodic arrays without invoking some way of suppressing or overcoming this fundamental shortcoming.

In this paper, we focus on thermocapillary patterning of thin liquid films and demonstrate how the phenomenon of resonant wavelength excitation, here induced by spatially periodic modulation of the thermal field, can lead to rapid and synchronous formation of highly uniform periodic arrays. The array pitch enforced by this modulation can also be selected to be much smaller than values obtained in comparable unmodulated systems.

## B. Organization of paper

The analysis presented in this work is organized as follows. Section II offers background and perspective relevant to the lithographic problem under study. Section III discusses various aspects of the general form of the thin-film equation for thermocapillary-driven flow in free surface films with arbitrary variation in temperature along the gas-liquid interface. Linear stability analysis of this so-called unmodulated system (i.e., flat solid boundaries maintained at constant separation and temperature difference) establishes important relations governing the wavelength and growth rate of the fastest growing mode. The expression for the critical wave number  $K_c$  defining the point of neutral stability is key to subsequent analysis. Section IV describes various aspects of the resonant wavelength analysis based on linear and weakly nonlinear film behavior induced by small amplitude, spatially periodic modulation of the thermal field. Section V outlines details of a Bloch wave analysis examining the stability of small amplitude equilibrium periodic states with  $K = K_{\text{ext}}$  that can form under certain conditions. Among other findings, the analysis yields an important expression for the critical modulation amplitude required to deform an initial liquid film into a uniform periodic array for a given ratio  $\mathcal{R} = K_{\text{ext}}/K_c$ .

Sections VI and VII respectively outline the numerical model and metrics used to quantify the dynamical behavior along with discussion of the results of direct numerical simulation for three types of modulation proposed. These results capture the dynamical behavior ranging from small (linear) to large (nonlinear) amplitude patterning of an initial flat liquid layer marked by a small degree of surface roughness modeled as white Gaussian noise. Behavior describing small amplitude arrays confirms the predictions in Secs. IV and V. Behavior for larger amplitude arrays offers additional insight into wave interference effects between the modes and higher harmonics triggered by the modulation and fundamental instability. Section VIII offers summary perspectives and concluding remarks.

## II. THERMOCAPILLARY LITHOGRAPHY: CHALLENGES AND A WAY FORWARD

### A. Early studies of thin-film instability and growth driven by large thermal gradients

Over two decades ago, Schäffer and coworkers [9–12] reported observation of localized arrays of microprotrusions in an initially flat molten polymeric nanofilm exposed to a large temperature gradient. They proposed that these formations develop in response to a long-wavelength instability due to gradients in acoustic phonon radiation pressure within the film. The supporting analysis was based on a system geometry in which a slender liquid film supported on a flat hot substrate is situated in close

proximity to a flat and parallel cold substrate. The analysis required that the temperature field vary only along the axis normal to the parallel substrates. For several reasons however, their experimental measurements and results turned out to be difficult to interpret. For example, the actual experimental setup consisted of a tilted plate geometry in which the two solid substrates maintained at a constant temperature differential were positioned at an angle to each other, thereby generating both vertical and horizontal thermal gradients. The horizontal thermal gradient, even if small, altered the peak amplitudes, growth rates, and pitch, making direct comparison to the theoretical model somewhat questionable. The emerging fluid protrusions were also allowed to grow until full contact with the cold substrate was achieved. Fluid reorganization and solidification upon contact with the cold substrate likely further altered the patterns due to physical effects not incorporated into the model. Additionally, while the predictions of the linear stability model are strictly predicated on early time growth to ensure only small amplitude deformation of an initial flat film, the measurements were taken at the final time once peak heights had contacted the opposing cold substrate.

Some years later, a different mechanism was proposed based on a long-wavelength thermocapillary instability [13–15]. Experiments [16–18] designed to better accord with key assumptions of that model were also conducted. Detailed measurements of the array pitch and peak growth rates at early times were found to be in good agreement with predictions of a linear stability analysis describing the competition between destabilizing thermocapillary forces promoting growth of protrusions and stabilizing capillary forces repressing formation of regions of high interfacial curvature. More recent theoretical work examining late time dynamics in the nonlinear regime has also demonstrated how fluid protrusions driven by significant thermocapillary stresses will sharpen in time due to a self-similar runaway process [19] that leads to cusplike shapes. Runaway dynamics leading to self-similar shapes is also known to occur in perfectly electrically conducting liquids subjected to strong electric field gradients [20,21].

The original thermocapillary model [13–15], to which we refer as the unmodulated system and reviewed in Sec. III, describes the configuration in which a gas-liquid bilayer is confined between two flat boundaries held at a constant separation distance and temperature differential. Experimental studies [16–18] testing predictions of that model utilized the design in Fig. 1(a). There, a molten polymeric nanofilm supported on a warmer silicon substrate was situated in close proximity (a few microns or less) to a transparent cylindrical disk (SU-8) attached to a colder cylindrical sapphire flat. The disk helped define a spatial region within which the vertical temperature gradient could be made quite large and more accurately controlled either by using thicker disks or thicker liquid films or thinner air gaps. The resulting large thermal

gradient was observed to trigger formation of multiple protrusions inspected directly by interference microscopy. In this way, spatiotemporal measurements of the distribution of peak heights, pitch, and growth rates were accurately obtained. Because thermocapillary flow in a single component fluid always draws liquid toward cooler regions of the gas-liquid interface, the taller protrusions whose tips were closer to the cooler substrate always grew more rapidly, a process leading to run away accelerated growth. The ultimate goal of studies such as these was to identify strategies for enforcing array formations with a prescribed pitch, shape, and peak height. If successful, it was anticipated that such a method of film patterning by noncontact means would be ideally suited to micro-optical applications because the protrusions emerge naturally within a liquid melt and will therefore exhibit molecularly smooth interfaces. This formation process contrasts sharply with patterning by conventional photolithographic methods that imbue films with highly roughened interfaces caused by multiple chemical etching steps required to add or remove material during film processing.

### B. Failure of lithographic patterning based solely on thermocapillary instability

Despite the seeming elegance of relying on an intrinsic hydrodynamic instability to generate periodic arrays, there remain notable challenges. The first difficulty stems from the very mechanism sustaining protrusion growth. Since taller peaks always advance more rapidly toward the cooler boundary, initial configurations marked by any disparities in film thickness, however small, will rapidly incur disparities in peak heights, shape, and pitch. Nonuniformities, such as in Fig. 1(b), are traceable to variations in initial film thickness incurred either during initial film preparation, deposition and annealing, or dewetting and pooling events around spacers used to enforce a fixed substrate separation distance or local film thickening during growth caused by coalescence of adjacent protrusions [16–18]. Unfortunately, experimental measurements have been very difficult to carry out for a number of reasons, including the fact that protrusion growth arising from nucleation of such film defects can interfere significantly with growth due to thermocapillary instability.

A second difficulty with thermocapillary lithography based solely on instability is related to achieving a reduction in the array pitch. As will be shown in Sec. III, the fastest growing wavelength in unmodulated systems is known to scale inversely as  $\Delta T_o^{-1/2}$  where  $\Delta T_o = T_+ - T_-$  is the applied temperature differential [see Fig. 1(a)]. In order to generate a large vertical thermal gradient, the parallel boundary substrates must be placed in very close proximity (a few microns or less) so as to minimize the separation distance  $d_o$ . Such proximity, however, causes effective cooling of the warmer substrate that tends

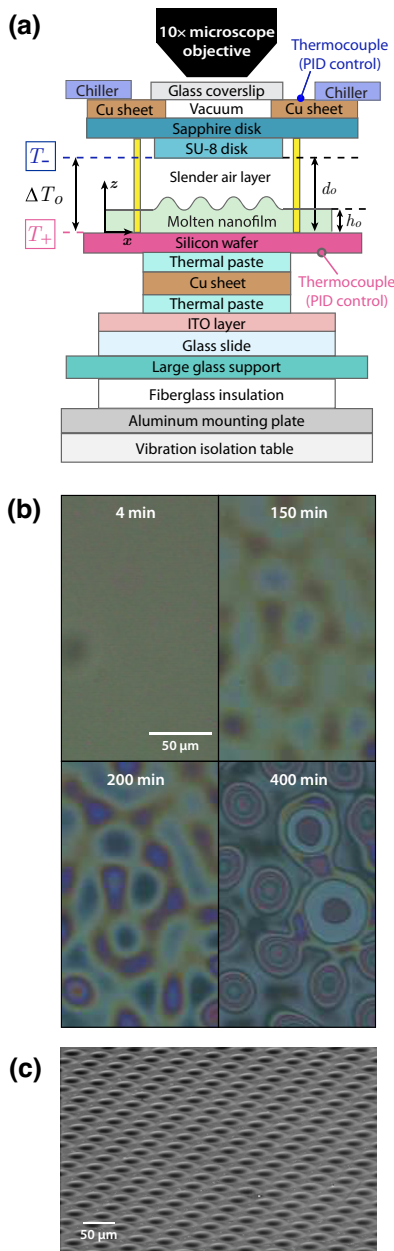


FIG. 1. (a) Unmodulated system for measurement of thermocapillary instability and growth in nanoscale films [16–18]. PID denotes the proportional integral derivative controller used for maintaining a fixed temperature. ITO denotes a surface layer of indium tin oxide. (b) Optical images showing variation in surface reflectivity due to emergent fluid protrusions. Images demonstrate significant nonuniformity in pattern pitch, shape, and height. High viscosity films, consisting of high molecular weight polystyrene, are used to slow the evolution process. (c) Scanning electron micrograph showing a solidified square microlens array resulting from a spatially periodically modulated thermal field enforced by a patterned colder substrate. Here, an initial 150-nm polymer melt film is exposed to an upper thin cold disk (SU-8) patterned by a square array of cylindrical pins (SU-8, not shown) with pitch  $50\ \mu\text{m}$ , pin diameter  $5\ \mu\text{m}$ , and pin length  $1.6\ \mu\text{m}$ . Further details are provided in Refs. [14,22].

to diminish the temperature difference  $\Delta T_o$ . As a result, experiments conducted so far have only achieved array pitch values of the order of tens of microns, too large for most micro-optical applications.

In preliminary experimental studies [22], it has been shown that highly uniform square arrays can be generated with a colder substrate that is patterned with a square array of long slender cylindrical pins. The microlens array shown in Fig. 1(c), which was solidified *in situ*, was measured to have a pitch closely matching that of the colder patterned substrate. The mystery resulting from those experiments, which provided the motivation for this current work, was that depending on the ratio  $\mathcal{R}$  and the length of the pins, the protrusions did not always align beneath the colder pins nor always generate uniform arrays.

### C. Resonant wavelength excitation phenomena in hydrodynamic systems

For several decades now, researchers have been investigating the phenomenon of resonant wavelength excitation in nonequilibrium systems as a way to induce frequency locking in the temporal domain. Wavelength locking in the spatial domain—as described in our current work—has also been studied but to a much lesser degree. This phenomena has been explored in the context of the Rayleigh-Bénard (RB) instability, known to occur in liquid layers that are sufficiently thick for gravitational forces to play a leading role. The RB instability, which induces density stratification in deep liquid layers heated from below, can generate periodic arrays of counter-rotating convective cells once the critical Rayleigh number is exceeded. In a seminal paper, Kelly and Pal [23] showed that, for wavelengths equal to the critical wavelength for onset of RB convection, the presence of small amplitude, spatially periodic modulation of the shape or temperature field of the boundary walls gives rise to resonant amplified cellular convection for any value of the Rayleigh number. A number of theoretical [24,25] and experimental studies [26,27], including references therein, have since explored spatiotemporal resonant response in spatially forced pattern-forming systems. These include, for example, the Swift-Hohenberg model for RB convection and the Lengyel-Epstein model for reaction diffusion kinetics leading to Turing patterns.

Higgins [28] reported observation of potential resonant wavelength excitation in a system involving dewetting of a nanoscale film. The dewetting process was observed to leave behind the receding front a periodic array of droplets. The pattern formation was believed to be caused by thermal fluctuations in the repulsive interaction between the liquid and supporting solid, modeled by a van der Waals interaction potential. The fluctuations were found to generate liquid pinholes that expanded rapidly due to the inertial-dominated dewetting process. The resulting



patterns strongly resembled similar spatial configurations seen in spinodal-like instabilities in binary fluids. Studies have since shown that this similarity stems from a mathematical similarity in the form of the equations governing these two processes [29]. In practice, dewetting patterns tend to exhibit significant nonuniformity in droplet peak heights, shape, and pitch.

It was later revealed from a bifurcation and stability analysis [30] describing thin-film dewetting from a substrate prepatterned with wetting and nonwetting stripes that sinusoidal modulation of the van der Waals interaction potential on a length scale comparable to the original instability wavelength can lead to highly uniform accelerated growth. This study shed light on an important feature of resonant excitation response, namely that the modulation immediately generates variations in film thickness equal to the modulation wavelength. This initial rippled state leads to an imperfect bifurcation that therefore expands the region of instability about the critical wavelength set by the unmodulated system. Apart from this one important study however, there appears to our knowledge no other work involving resonant wavelength excitation phenomena in thin liquid films.

### III. GENERAL EQUATION FOR THERMOCAPILLARY GROWTH OF PROTRUSIONS IN SLENDER LIQUID FILMS

In this paper, we explore the consequences of resonant wavelength excitation in thin films prone to thermocapillary instability. These excitations are triggered by a spatially periodic modulated thermal field enforced in one of three ways, as depicted in Fig. 2. In this section, we outline the derivation leading to the *general* form of the thin-film equation applicable to any system undergoing variation of the temperature along the gas-liquid interface. We then briefly review known results for the instability wavelength and growth rate in unmodulated systems in order to establish some important relations such as the expression for the critical wavelength  $K_c$ , a key parameter for the analysis of modulated systems presented in Sec. IV and thereafter.

The general thin-film equation [15,31] relevant to this study is predicated on a number of important approximations listed here. It is assumed that the liquid flux governing protrusion growth is dominated by large thermocapillary and capillary forces, which far exceed any contribution from gravitational leveling. The velocity and pressure fields within the thin liquid film satisfy the long-wavelength approximation in which the vertical length scale is much smaller than the horizontal length scale—as a result, the viscous forces are orders of magnitude larger than inertial forces, which are neglected. The small geometric aspect ratio also ensures that the thermal flux is dominated solely by thermal conduction along the slender (vertical) direction. Since the vertical length scale is

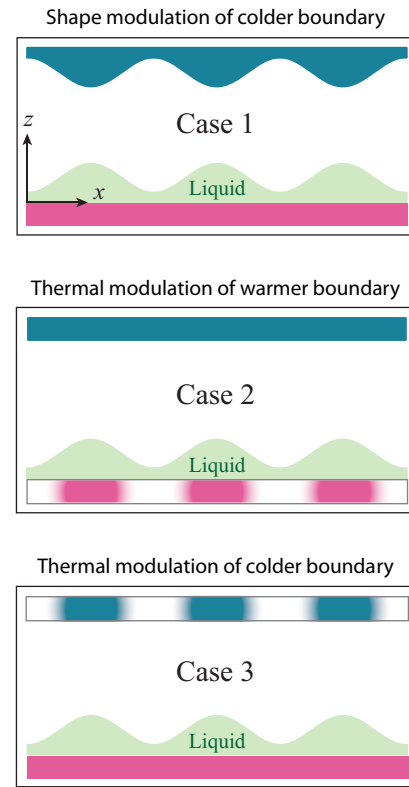


FIG. 2. Schematic diagram showing the three types of spatially periodic thermal modulation examined in this work. Darker stripes signify cooler regions of modulated boundaries.

very small by design, all material constants pertaining to the gas and liquid layers are assumed to have constant values except for the liquid surface tension that varies with temperature along the gas-liquid interface. The insulating nature of the gas layer plays a significant role in establishing large variations in temperature along the gas-liquid interface due to variations in the liquid film thickness. The liquid film is also assumed to comprise an incompressible Newtonian fluid, which is not a severe restriction since estimated flow shear rates are too small to induce non-Newtonian response even in polymer melt films.

The dimensionless thin-film equation describing the competition between thermocapillary and capillary forces along the liquid interface is given by

$$\frac{\partial H}{\partial \tau} + \frac{\partial}{\partial X} \left( \frac{H^3}{3} \frac{\partial^3 H}{\partial X^3} - \mathcal{M} \frac{H^2}{2} \frac{\partial \Theta_H}{\partial X} \right) = 0. \quad (1)$$

Here,  $H(X, \tau)$  denotes the local film thickness and  $\Theta_H(X, \tau) \equiv \Theta[X, Z = H(X, \tau)]$  denotes the temperature variation along the free surface  $Z = H(X, \tau)$ . The dimensionless number  $\mathcal{M} = \text{Ma} \times \text{Ca} = \gamma_T \Delta T_o / (\epsilon^2 \gamma)$  specifies the ratio of thermocapillary to capillary liquid flux. Details of the full derivation leading to this form can be found in Refs. [13–15]. Relevant scalings used in our

TABLE I. Variable definitions and scalings for the thin-film thermocapillary model described in the text. Material constants are typically evaluated at the average temperature of the warmer substrate surface. For systems subject to spatially periodic modulation as depicted in Fig. 2, the variables  $D_o$  and  $\Delta T_o$  refer to values averaged over one wavelength of the modulation period.

Material constant	Symbol	
Liquid density	$\rho$	
Liquid viscosity	$\mu$	
Liquid heat capacity	$c_p$	
Thermal conductivity ratio	$\kappa = k_{\text{air}}/k_{\text{liq}} < 1$	
Liquid thermocapillary coefficient	$\gamma_T =  \partial\gamma/\partial T $	
Dimensional variable	Characteristic scale	Dimensionless variable
Initial liquid thickness	$h_o$	
Intrinsic instability wavelength	$l_o = \lambda_{\text{max}}$	
Small aspect ratio		$\epsilon^2 = (h_o/l_o)^2 \ll 1$
Perturbation variables		$\tilde{\epsilon} \ll 1$ $\epsilon \ll 1$ $\delta \ll 1$
Geometric scales	$x_o = l_o$ $z_o = h_o$	$X = x/x_o$ $Z = z/z_o$
Interface height	$z_o = h_o$	$H = h(x, t)/z_o$
Boundary separation distance	$z_o = h_o$	$D = d(x)/z_o$
Wave numbers	$k_o = 2\pi/l_o$	$D_o = d_o/h_o$ $K_{\text{max}} = k_{\text{max}}/k_o$ $K_c = k_c/k_o$ $K_{\text{ext}} = k_{\text{ext}}/k_o$ $Q = q/k_o$ $\mathcal{R} = K_{\text{ext}}/K_c$
External modulation ratio		
Horizontal flow velocity	$u_o = \epsilon^3(\gamma/\mu)$	$U = u/u_o$
Vertical flow velocity	$w_o = \epsilon^4(\gamma/\mu)$	$W = w/w_o$
Time	$t_o = l_o/u_o$	$\tau = t/t_o$
Flow pressure	$p_o = \mu u_o/\epsilon h_o$	$P = p/p_o$
Temperature drop	$\Delta T_o = T_+ - T_-$	$\Theta = (T - T_-)/\Delta T_o$
Dimensionless number	Symbol	Value
Prandtl	Pr	$\mu c_p/k_{\text{liq}}$
Reynolds	Re	$\rho u_o z_o/\mu$
Capillary	Ca	$\mu u_o/(\epsilon^3 \gamma)$
Marangoni	Ma	$\epsilon \gamma_T \Delta T_o/(\mu u_c)$
Surface force ratio	$\mathcal{M} = \text{Ma} \times \text{Ca}$	$\gamma_T \Delta T_o/(\epsilon^2 \gamma)$

current study for nondimensionalization of equations and other relations are listed in Table I.

The slender limit geometry enforces the long-wavelength approximation that introduces the two small expansion ratios  $\epsilon^2 \ll 1$  and  $\epsilon \text{RePr} \ll 1$ —see Table I. As a result, the heat transfer within the air-liquid bilayer simply

reduces to a system characterized by 1D thermal conduction. The temperature field along the free surface can therefore be obtained by solution of the 1D Laplace equation  $\partial^2 \Theta/\partial Z^2 = 0$ , whose four unknown constants are determined from the boundary conditions imposed at the warmer ( $Z = 0$ ) and cooler ( $Z = D$ ) substrates and the requirement of continuity in the temperature and thermal flux field at the moving interface, i.e.,  $\Theta_{\text{air}}|_H = \Theta_{\text{liquid}}|_H$  and  $\kappa(\partial\Theta_{\text{air}}/\partial Z)_H = (\partial\Theta_{\text{liquid}}/\partial Z)_H$ . The temperature distribution along the free surface is given by

$$\Theta_H(X, \tau) \equiv \Theta[X, Z = H(X, \tau)] = \frac{\kappa H(X, \tau)\Theta(X)|_{Z=D(X)} + [D(X) - H(X, \tau)]\Theta(X)|_{Z=0}}{[D(X) - (1 - \kappa)H(X, \tau)]}. \quad (2)$$

Variations in the temperature field with time along the moving interface occur in response to variations in film thickness caused by hydrodynamic flow.

### A. Review of the linear instability wavelength and growth rate in unmodulated systems

Before examining systems subject to periodic modulation of the temperature field, we first outline key results pertaining to unmodulated systems, defined by flat solid boundaries held at a constant separation distance  $D(X) = D_o$  and constant temperature differential where  $\Theta_+(Z = 0) = 1$  and  $\Theta_-(Z = D_o) = 0$ . Equations (1) and (2) then combine to give the governing nonlinear fourth-order equation:

$$\frac{\partial H}{\partial \tau} + \frac{\partial}{\partial X} \left\{ \frac{H^3}{3} \frac{\partial^3 H}{\partial X^3} + \frac{\kappa D_o \mathcal{M} H^2}{2[D_o - (1 - \kappa)H]^2} \frac{\partial H}{\partial X} \right\} = 0. \quad (3)$$

The terms in brackets represent the total fluid flux from capillary and thermocapillary flows, respectively. A first-order perturbation analysis of Eq. (3) about a uniform base state where  $H(X, \tau) = 1 + \tilde{\epsilon} \tilde{H}(X, \tau)$  and  $\tilde{\epsilon} \ll 1$  yields the linearized fourth-order equation given by [13, 15]

$$\frac{\partial \tilde{H}}{\partial \tau} + \frac{1}{3} \frac{\partial^4 \tilde{H}}{\partial X^4} + \frac{\kappa D_o \mathcal{M}}{2(D_o + \kappa - 1)^2} \frac{\partial^2 \tilde{H}}{\partial X^2} = 0. \quad (4)$$

Throughout this work, we focus exclusively on periodic disturbances, whose general solution for the unmodulated system is

$$\tilde{H}(X, \tau) = \sum_{n=0}^{\infty} e^{\beta_n \tau} [a_n \cos(K_n X) + b_n \sin(K_n X)], \quad (5)$$

where

$$\beta_n = \left( \frac{\kappa D_o \mathcal{M}}{2(D_o + \kappa - 1)^2} - \frac{K_n^2}{3} \right) K_n^2 \quad (6)$$

and

$$K_n = 2\pi n \quad \text{for } n = 0, 1, 2, \dots \quad (7)$$

This disturbance solution can also be re-expressed as

$$H(X, \tau) = 1 + \tilde{\epsilon} \sum_{n=0}^{\infty} e^{\beta_n \tau} \cos(2\pi n X + \phi_n), \quad (8)$$

where the phase constants  $\phi_n$  are determined by the initial condition.

The quadratic term in Eq. (6), which can be made very large and reflects growth of protrusions by thermocapillary forces, is counteracted by the quartic term, which reflects the leveling action of capillary forces and is especially large in regions of high interfacial curvature, such as the tips of protrusions or indentations in the interstitial regions. This competition in surface forces generally leads to the dispersion curve in Fig. 3 characterizing all type-II instabilities [32]. The fastest growing mode  $K_{\max}$  is determined from the relation

$$K_{\max} = \sqrt{\frac{3\kappa D_o \mathcal{M}}{4(D_o + \kappa - 1)^2}}, \quad (9)$$

and the corresponding maximum growth rate is given by

$$\beta_{\max} = \frac{3}{16} \frac{(\kappa D_o \mathcal{M})^2}{(D_o + \kappa - 1)^4}. \quad (10)$$

A key wave number for the analysis to follow is  $K_c$ , which represents the point of marginal stability, i.e.,  $\beta(K) = 0$  for  $K \neq 0$ , as indicated in Fig. 3:

$$K_c = \sqrt{2} K_{\max} = \sqrt{\frac{3\kappa D_o \mathcal{M}}{2(D_o + \kappa - 1)^2}}. \quad (11)$$

The governing linearized equation for early time disturbance growth can therefore be rewritten as

$$\frac{\partial \tilde{H}}{\partial \tau} + \frac{1}{3} \frac{\partial^4 \tilde{H}}{\partial X^4} + \frac{K_c^2}{3} \frac{\partial^2 \tilde{H}}{\partial X^2} = 0. \quad (12)$$

In Sec. IV, we examine more closely the dynamics in the vicinity of  $K_c$  for systems subject to spatially periodic boundary modulation.

In contrast to onset of a RB instability, which only occurs if the critical Rayleigh number is exceeded, the dispersion equation for the long-wavelength thermocapillary instability given by Eq. (9) reveals that there is no critical value for  $\mathcal{M}$ . That is, an initial flat film will undergo thermocapillary instability no matter how small the value  $\mathcal{M}$  [33]. Periodic deformations of the moving interface

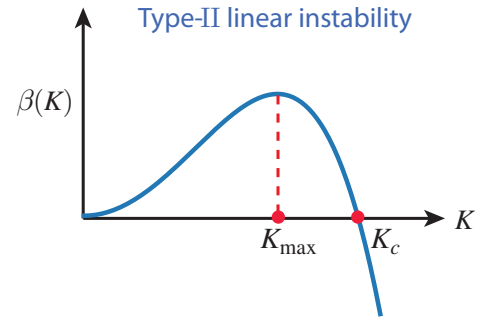


FIG. 3. Disturbance growth rate  $\beta(K)$  (dimensionless form) for the long-wavelength thermocapillary instability for a slender gas-liquid bilayer confined between flat boundaries held at constant separation and temperature difference. The dispersion relation is of type II, where  $K_{\max}$  is the wave number of the fastest growing unstable mode. Thermocapillary forces promote growth for  $K < K_c$  while capillary forces repress growth for  $K > K_c$ , where  $K_c$  denotes the wave number of the marginally stable state.

therefore always occur no matter how small the temperature differential  $\Delta T_o$ . The smaller the value  $\Delta T_o$ , of course, the smaller the value  $K_{\max}$  and therefore the larger the value of the array pitch.

Reverting to the dimensional form of the most unstable wavelength, the achievable pattern pitch for small-scale periodic deformation of an initial flat film is given by

$$\lambda_{\max} = 2\pi h_o \sqrt{\frac{4\gamma h_o}{3\kappa d_o \gamma_T \Delta T_o} \left( \frac{d_o}{h_o} + \kappa - 1 \right)}. \quad (13)$$

Optical measurements of early time growth and pitch formation [17,18] for small clusters of protrusion arrays demonstrate good agreement with the prediction from Eq. (13). As discussed in the Introduction, however, the patterns still exhibit nonuniformities and lack true long-range order. In what follows, we demonstrate how resonant excitation triggered by spatial boundary modulation can be used to generate highly uniform arrays with a smaller pitch set by the modulation wavelength  $2\pi/k_{\text{ext}}$  and not the instability wavelength  $\lambda_{\max}$ .

#### IV. RESONANT WAVELENGTH ANALYSIS FOR CASE 1, 2, AND 3 MODULATION

For simplicity, we restrict analysis in this paper to systems involving either shape or thermal modulation of one boundary. Thermal modulation of the liquid interface temperature is achieved either by spatial periodic modulation of the cooler boundary surface where  $D(X) = D_o[1 + \delta \cos(K_{\text{ext}}X)]$ , which we coin case 1 systems, or thermal modulation of one of the flat boundaries with  $\Theta_+(X) = 1 + \delta \cos(K_{\text{ext}}X)$  (case 2) or  $\Theta_-(X) = \delta \cos(K_{\text{ext}}X)$  (case 3). Since we seek arrays with a finer pitch than  $\lambda_{\max}$  in unmodulated systems, we restrict attention to the range  $K_{\text{ext}} > K_c$ .

For case 1 systems, the thermal boundary conditions are given by

$$\Theta_+(X) = \Theta(X, Z = 0) = 1, \quad (14)$$

$$\Theta_-(X) = \Theta(X, Z = D(X)) = 0. \quad (15)$$

According to Eq. (2), the temperature distribution along the free interface reduces to the form

$$\Theta_H(X, \tau) = \frac{D(X) - H(X, \tau)}{D(X) - (1 - \kappa)H(X, \tau)}, \quad (16)$$

which when substituted into Eq. (1) gives

$$\begin{aligned} \frac{\partial H}{\partial \tau} + \frac{\partial}{\partial X} \left\{ \frac{H^3}{3} \frac{\partial^3 H}{\partial X^3} \right\} \\ + \frac{\partial}{\partial X} \left\{ \frac{\kappa \mathcal{M} H^2}{2[D - (1 - \kappa)H]^2} \left( D \frac{\partial H}{\partial X} - H \frac{\partial D}{\partial X} \right) \right\} = 0. \end{aligned} \quad (17)$$

For this case, the term  $\partial \Theta_H / \partial X$  in Eq. (1) gives rise to two sources of thermocapillary flow. The first is generated by variations in the local film thickness  $H(X, \tau)$  and the second is generated by the thermal field imprinted onto the film from the corrugated topography  $D(X)$  of the colder boundary. As expected, the competition between the length scale  $K_c^{-1}$  set by the intrinsic instability and that set by the modulation length scale  $K_{\text{ext}}^{-1}$  leads to complex and nonlinear wave interactions. As we shall see, final liquid configurations can either exhibit disordered arrays with highly nonuniform pitch, shapes, and peak heights that do not align with the cooler regions of the modulated substrate or desirable, rapid, and highly synchronized growth leading to uniform periodic arrays.

### A. Linear stability analysis

We first consider the limit of small amplitude modulation of the colder boundary such that  $D(X) = D_o[1 + \delta \cos(K_{\text{ext}}X)]$  with  $\delta \ll 1$ . A perturbation expansion of Eq. (17) with  $H(X) = 1 + \delta H_p(X, \tau)$  yields the linearized fourth-order equation incorporating thermal modulation given by

$$\frac{\partial H_p}{\partial \tau} + \frac{1}{3} \frac{\partial^4 H_p}{\partial X^4} + \frac{K_c^2}{3} \frac{\partial^2 H_p}{\partial X^2} = -\frac{K_c^2 K_{\text{ext}}^2}{3} \cos(K_{\text{ext}}X), \quad (18)$$

where  $K_c$  is defined by Eq. (11). The homogeneous solution is identical to that derived earlier for Eq. (12). The

general solution to  $\mathcal{O}(\delta)$  is then

$$\begin{aligned} H(X, \tau) = 1 + \delta \sum_{n=0}^{\infty} e^{\beta_n \tau} \cos(2\pi nX + \phi_n) \\ - \delta \cos(K_{\text{ext}}X) \frac{K_c^2}{K_{\text{ext}}^2 - K_c^2} \\ \times (1 - e^{-K_{\text{ext}}^2(K_{\text{ext}}^2 - K_c^2)\tau/3}), \end{aligned} \quad (19)$$

where the growth rate given by Eq. (6) can be re-expressed as

$$\beta_n = \frac{1}{3}(K_c^2 - K_n^2)K_n^2, \quad (20)$$

where  $K_n = 2\pi n$  for  $n = 0, 1, 2, \dots$ . The phase constants  $\phi_n$  are determined from the initial condition. This solution, of course, is no longer valid when the second term approaches a value of the order  $1/\delta$ , or equivalently when  $\tau \gtrsim \beta_{\text{max}}^{-1} \ln \delta^{-1}$ .

Equation (19) describes interface evolution by two processes characterized by different time constants, namely growth by the intrinsic instability with time constant  $\beta_{\text{max}}^{-1}$  given by Eq. (10) and resonant growth due to thermal modulation with a time constant

$$\tau_{\text{ext}} = \frac{3}{K_{\text{ext}}^2(K_{\text{ext}}^2 - K_c^2)}. \quad (21)$$

In general, disturbance evolution according to Eq. (19) is expected to manifest disordered growth, leading to nonuniformity in protrusion pitch, amplitude, and shape. However, for parameter values  $\beta_n < 0$  and  $K_{\text{ext}} > K_c$ , the interface height is expected to attain a saturated resonant state of the form

$$H(X) = 1 - \delta \left( \frac{K_c^2}{K_{\text{ext}}^2 - K_c^2} \right) \cos(K_{\text{ext}}X). \quad (22)$$

### B. Multiple scales analysis about $K_c$

The influence of weakly nonlinear behavior due to wave interactions between the thermocapillary instability and the spatially periodic modulation can be further examined by carrying out a multiple scales expansion near  $K_c$  based on the two time scales above. To that end, we introduce the stretched time scale  $\tau' = \varepsilon^2 \tau$  and, as customary [34], treat the variables  $\tau$  and  $\tau'$  as independent quantities. The interface function is then expanded according to

$$\begin{aligned} H(\xi, \tau) = 1 + \varepsilon H_1(\xi, \tau, \tau') + \varepsilon^2 H_2(\xi, \tau, \tau') \\ + \varepsilon^3 H_3(\xi, \tau, \tau'), \end{aligned} \quad (23)$$

where  $\xi = K_{\text{ext}}X$  and  $\varepsilon \ll 1$ . Substitution of the relation  $\tau = \tau'/\varepsilon^2$  into the exponent of the last term in Eq. (19)



reveals the scaling

$$(K_{\text{ext}} - K_c)/K_c = \varepsilon^2 \alpha, \quad (24)$$

where the constant  $\alpha > 0$ . Inserting this relation into the amplitude of the last term of Eq. (19) reveals that the amplitude coefficient scales as  $\delta/\varepsilon^2$ . Since this term represents a first-order disturbance proportional to  $\varepsilon$ , it must then be the case that  $\delta$  scales as  $\varepsilon^3$ , which without loss of generality is defined to be

$$\delta = \varepsilon^3. \quad (25)$$

The perturbative solution through order  $\varepsilon^3$  is obtained by substituting the expansion in Eq. (23) into Eq. (17) recast in terms of  $\xi$ , subject to the spatially periodic condition  $H(\xi = 0, \tau, \tau') = H(\xi = K_{\text{ext}} = 2\pi, \tau, \tau')$ . The original time derivative then expands into two separate terms describing fast and slow dynamics, according to which

$$\begin{aligned} \frac{\partial H}{\partial \tau} &\rightarrow \left( \frac{\partial}{\partial \tau} + \frac{\partial}{\partial \tau'} \frac{\partial \tau'}{\partial \tau} \right) (1 + \varepsilon H_1 + \varepsilon^2 H_2 + \varepsilon^3 H_3) \\ &= \varepsilon \frac{\partial H_1}{\partial \tau} + \varepsilon^2 \frac{\partial H_2}{\partial \tau} + \varepsilon^3 \left( \frac{\partial H_3}{\partial \tau} + \frac{\partial H_1}{\partial \tau'} \right). \end{aligned} \quad (26)$$

Accordingly, the governing equation to order  $\varepsilon$  is

$$\frac{\partial H_1}{\partial \tau} + \frac{K_c^4}{3} \mathcal{L}\{H_1\} = 0, \quad (27)$$

where

$$\mathcal{L} = \left( \frac{\partial^4}{\partial \xi^4} + \frac{\partial^2}{\partial \xi^2} \right), \quad (28)$$

whose general solution is

$$\begin{aligned} \frac{\partial H_3}{\partial \tau} + \frac{K_c^4}{3} \mathcal{L}\{H_3\} &= -\frac{K_c^4}{3} \cos \xi + Q_1(\tau') \frac{d\Phi_1}{d\tau'} \sin[\xi + \Phi_1(\tau')] \\ &\quad - \left[ \frac{dQ_1}{d\tau'} + \frac{2\alpha}{3} K_c^4 Q_1(\tau') - \left( \frac{22B^2 - 16B + 7}{72} K_c^4 Q_1^3(\tau') \right) \right] \cos[\xi + \Phi_1(\tau')] \\ &\quad + \frac{2}{3} (2B - 1) K_c^4 Q_1(\tau') Q_2(\tau') \cos[2\xi + \Phi_1(\tau') + \Phi_2(\tau')] \\ &\quad + \frac{10B^2 - 8B + 3}{8} K_c^4 Q_1^3(\tau') \cos[3\xi + 3\Phi_1(\tau')] + G(\xi, \tau), \end{aligned} \quad (33)$$

where  $G$  represents the contribution dependent on the unstretched time scale and  $\alpha$  is given by Eq. (24). Since the functions  $\sin \xi$  and  $\cos \xi$  are solutions of the homogenous equation  $\mathcal{L}\{H_3\} = 0$ , such terms give rise to contributions in  $H_3$  proportional to  $\xi \sin \xi$  and  $\xi \cos \xi$ , which do not satisfy the periodic boundary condition. As a result, the sum of coefficients on the right-hand side of Eq. (33), which are separately proportional to  $\sin \xi$  and  $\cos \xi$ , must both sum to zero. These summation conditions yield the requirements  $d\Phi_1/d\tau' = 0$  and

$$\begin{aligned} H_1(\xi, \tau, \tau') &= Q_1(\tau') \cos[\xi + \Phi_1(\tau')] \\ &\quad + \sum_{n=2}^{\infty} a_{1,n} \cos(n\xi + \phi_{1,n}) e^{-n^2(n^2-1)K_c^4 \tau/3}. \end{aligned} \quad (29)$$

Proceeding similarly, the governing equation for  $H_2(\xi, \tau, \tau')$  is

$$\begin{aligned} \frac{\partial H_2}{\partial \tau} + \frac{K_c^4}{3} \mathcal{L}\{H_2\} &= (2B - 1) \frac{K_c^4}{3} Q_1^2(\tau') \\ &\quad \times \cos[2\xi + 2\Phi_1(\tau')] + F(\xi, \tau), \end{aligned} \quad (30)$$

where  $F$  represents the contribution dependent on the unstretched variable  $\tau$ . The constant  $B$  given by

$$B = \frac{1 - \kappa}{D_o + \kappa - 1} > 0 \quad (31)$$

is set by the relevant geometric and material parameters and is always positive since  $D_o > 1$  and  $0 < \kappa < 1$ . The general solution to order  $\varepsilon^2$  is

$$\begin{aligned} H_2(\xi, \tau, \tau') &= \frac{2B - 1}{12} Q_1^2(\tau') \cos[2\xi + 2\Phi_1(\tau')] \\ &\quad + Q_2(\tau') \cos[\xi + \Phi_2(\tau')] + \tilde{F}(\xi, \tau), \end{aligned} \quad (32)$$

where  $\tilde{F}$  represents the contribution that decays exponentially in proportion to  $\tau$ . As expected, periodic modulation triggers the onset of both the fundamental and second harmonic responses.

Solution of the amplitude function  $Q_1(\tau')$  requires expansion to order  $\varepsilon^3$ . Substitution of the functions  $H_1$  and  $H_2$  into Eq. (17) yields the governing equation

$$\frac{dQ_1}{d\tau'} = K_c^4 \left( c_3 Q_1^3 - \frac{2}{3} \alpha Q_1 - c_0 \right), \quad (34)$$

where  $c_0$  and  $c_3$  represent the positive constant values

$$c_0 = \frac{1}{3}, \quad (35)$$

$$c_3 = \frac{22B^2 - 16B + 7}{72} = \frac{2D_o^2 + 45(D_o/3 + \kappa - 1)^2}{72(D_o + \kappa - 1)^2}, \quad (36)$$

with the choice  $\Phi_1 = 0$  since the origin of time is arbitrary. Equation (33) then reduces to

$$\begin{aligned} \frac{3}{K_c^4} \frac{\partial H_3}{\partial \tau} + \mathcal{L}\{H_3\} \\ = 2(2B - 1)Q_1(\tau')Q_2(\tau') \cos[2\xi + \Phi_2(\tau')] \\ + \frac{3}{8}[10B^2 - 8B + 3]Q_1^3(\tau') \cos(3\xi) + G(\xi, \tau), \end{aligned} \quad (37)$$

whose solution is

$$\begin{aligned} H_3(\xi, \tau, \tau') = Q_3(\tau') \cos[\xi + \Phi_3(\tau')] \\ + \frac{2B - 1}{6} Q_1(\tau')Q_2(\tau') \cos[2\xi + \Phi_2(\tau')] \\ + \frac{10B^2 - 8B + 3}{192} Q_1^3(\tau') \cos(3\xi) + \tilde{G}(\xi, \tau). \end{aligned} \quad (38)$$

While this solution exhibits third harmonic response in phase with the external forcing, it also includes phase-delayed contributions from the first and second harmonics. The solution  $H(\xi, \tau, \tau')$  in the limit  $K_{\text{ext}} \rightarrow K_c$  up through order  $\varepsilon^3$  therefore describes interface shapes both in and out of phase with the wave number  $K_{\text{ext}}$ , which will in general elicit disordered growth. In the section that follows, however, we demonstrate parameter ranges that lead to highly synchronous growth.

To conclude this section, we note that a multiple scales analysis as  $K \rightarrow K_c$  was also conducted for the unmodulated case described in Sec. III A. That analysis yields the identical relation given by Eq. (34) with  $c_0 = 0$ .

### C. Stability of equilibrium solutions about $K_c$

According to Eq. (29), the solution for small amplitude disturbances as  $K_{\text{ext}} \rightarrow K_c$  for case 1 systems is given by  $\varepsilon$ ,

$$H_1(X, \tau') = 1 + \varepsilon Q_1(\tau') \cos(K_{\text{ext}}X). \quad (39)$$

We now seek stable equilibrium solutions with  $dQ_1/d\tau' = 0$  given by the cubic roots of Eq. (34). The criterion for stability can be found by substitution of the

expansion  $Q_1(\tau') = \bar{Q}_1 + \Delta Q_1(\tau')$  into Eq. (34) where  $\Delta Q_1(\tau') \ll 1$ :

$$\frac{1}{\Delta Q_1} \frac{d\Delta Q_1}{d\tau'} = K_c^4 \left( 3c_3 \bar{Q}_1^2 - \frac{2\alpha}{3} \right). \quad (40)$$

Stable equilibrium solutions satisfy the inequality  $\bar{Q}_1^2 < 2\alpha/(9c_3)$ , where  $\alpha > 0$  and  $c_3 > 0$ , as shown previously. Consequently, for a specified value  $\alpha$ , which scales linearly with the ratio  $K_{\text{ext}}/K_c$ , there exists an upper bound on the corrugation amplitude  $\bar{Q}_1(\alpha)$  below which periodic solutions are linearly stable and above which they undergo rapid growth. The coupled set of equations governing the stability boundary are

$$c_3 \bar{Q}_1^3 - \frac{2}{3} \alpha \bar{Q}_1 - c_0 = 0, \quad (41)$$

$$3c_3 \bar{Q}_1^2 - \frac{2\alpha}{3} = 0, \quad (42)$$

which yield only one pair of real solutions  $\{\bar{Q}_1^*, \alpha^*\}$ . The linear stability of small amplitude periodic equilibrium states therefore requires

$$|\bar{Q}_1| < |\bar{Q}_1^*| = \left( \frac{c_0}{2c_3} \right)^{1/3}, \quad (43)$$

$$\alpha > \alpha^* = 9 \left( \frac{c_0^2 c_3}{32} \right)^{1/3}. \quad (44)$$

We note that, since  $\bar{Q}_1^* < 0$ , stable equilibrium solutions given by Eq. (39) represent corrugated film shapes that are  $\pi$  out of phase with the modulation function  $D(X)$ . This is to be expected since thermocapillary flow acts in such a way that those portions of the boundary profile  $D(X)$  closer to the liquid interface induce cooling with an increase in surface tension in regions of immediate vicinity. In turn, fluid is drawn to those cooler regions, causing growth of protrusions and an interface configuration resembling an inversion of the boundary shape  $D(X)$ .

Shown in Fig. 4 is a comparison of the bifurcation diagram  $\bar{Q}_1(\alpha)$  for the unmodulated system [i.e.,  $D(X) = D_o$ ] and case 1 modulation subject to an identical average substrate temperature difference. As evident, the unmodulated system exhibits a perfect forward bifurcation—the latter an imperfect one.

As was shown in Sec. IV B, the relation between the amplitude of the boundary modulation and the resulting modulation amplitude of the liquid film is given by  $\delta = \varepsilon^3$ . This identity can be used to relate the bifurcation parameter  $\alpha^*$  to the critical modulation amplitude  $\delta^*$  below which a steady, small amplitude periodic equilibrium state can be

achieved, namely,

$$\begin{aligned}\delta < \delta^* &= (\alpha^*)^{-3/2} \left( \frac{K_{\text{ext}}}{K_c} - 1 \right)^{3/2} \\ &= \frac{1}{27} \sqrt{\frac{32}{c_0^2 c_3}} \left( \frac{K_{\text{ext}}}{K_c} - 1 \right)^{3/2},\end{aligned}\quad (45)$$

where  $c_0$  and  $c_3$  are given by Eqs. (35) and (36), respectively. For  $\delta < \delta^*$ , the initial flat film will rapidly adopt the small amplitude equilibrium shape  $H_1(X) = 1 + \varepsilon Q_1 \cos(K_{\text{ext}}X)$  that can persist for some time. For  $\delta > \delta^*$ , the initial film will also develop periodic protrusions, but these will accelerate ever more rapidly toward the colder boundary until a peak makes contact with the colder boundary or a valley makes contact with the warmer boundary. In Sec. VII E, we directly compare the critical values estimated from Eq. (45) against results extracted from direct numerical simulation.

The analysis in this section suggests the existence of a parameter range for which the amplitude  $Q_1$  governing the growth of  $H_1$  is time independent and the solution linearly stable. However, this does not preclude time-dependent behavior from the progressively smaller contributions  $H_2(\xi, \tau, \tau')$  or  $H_3(\xi, \tau, \tau')$ . By continuation of the expansion procedure utilized above, we confirmed that  $Q_2$

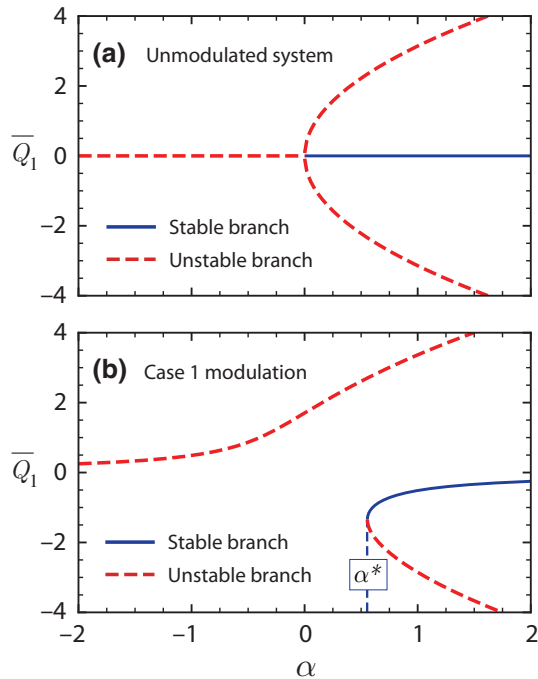


FIG. 4. Solutions to Eq. (41) for the equilibrium amplitude  $\bar{Q}_1(\alpha)$  for identical average substrate temperature and separation distance for  $\kappa = 1/4$  and  $D_o = 5$ . Shown are results for (a) an unmodulated system and (b) a case 1 system. Bifurcation coordinate  $(\alpha^*, \bar{Q}_1^*)$ : (a) (0, 0) and (b) (0.554958, -1.35145).

TABLE II. Spatial and thermal boundary conditions where  $F(X) = \cos(K_{\text{ext}}X)$  and  $\delta \ll 1$ . The coefficient values  $\Upsilon$  are required for the entries in Table III.

	Separation gap $D(X)/D_o$	Substrate temperatures	Coefficient value $\Upsilon$
Case 1	$1 + \delta F(X)$	$\Theta_+ = 1$ $\Theta_- = 0$	1
Case 2	1	$\Theta_+ = 1 + \delta F(X)$ $\Theta_- = 0$	$\frac{(D_o + \kappa - 1)(D_o - 1)}{\kappa D_o}$
Case 3	1	$\Theta_+ = 1$ $\Theta_- = \delta F(X)$	$\frac{(D_o + \kappa - 1)}{D_o}$

undergoes exponential decay in time on the stable branch of  $Q_1$ ; however, no such demonstration was possible for  $Q_3$  to order  $\varepsilon^5$ . As for the phase functions, we confirmed that  $\Phi_2$  remains time independent to order  $\varepsilon^4$  and  $\Phi_3$  time independent to order  $\varepsilon^5$ .

In Sec. VII devoted to direct numerical simulations, we demonstrate that initial conditions describing a flat film with small amplitude surface roughness preclude formation of truly stationary periodic states. However, there can occur a sustained period in time marked by the emergence of quasistationary patterns that grow extremely slowly. For convenience, we refer to these intermediate time, small amplitude quasistationary states as saturated periodic states. The stability of such states is investigated in depth in Sec. V using Bloch wave analysis.

#### D. Linear stability and multiple scales analysis generalized to cases 2 and 3

In the previous section, we focused exclusively on case 1 modulation. The analysis presented can be extended to case 2 and 3 modulation as well. The general analysis leads to changes in the values of certain coefficients in the boundary conditions and subsequent relations. Summaries of these modifications applicable to all three cases depicted in Fig. 2 are provided in Tables II and III. The coefficients  $\Upsilon$  depend only on the ratio of gas to liquid thermal conductivities  $\kappa$  and the geometric constant  $D_o$  representing the average solid boundary separation distance.

TABLE III. Modified coefficient values for generalization of equations to case 1, 2 and 3 modulation.

	$\Upsilon$ modified coefficient values
Equation (18)	$\cos(K_{\text{ext}}X) \rightarrow \Upsilon \cos(K_{\text{ext}}X)$
Equation (19)	$\cos(K_{\text{ext}}X) \rightarrow \Upsilon \cos(K_{\text{ext}}X)$
Equation (33)	$-\cos \xi \rightarrow -\Upsilon \cos \xi$
Equation (35)	$1/3 \rightarrow \Upsilon/3$

## V. GENERAL BLOCH WAVE ANALYSIS

In Sec. IV, it was demonstrated how spatial modulation of the thermal field can elicit quasistationary periodic formations with periodicity  $2\pi/K_{\text{ext}}$  at early to intermediate times. We next establish necessary conditions for such periodic states satisfying  $H_o(X) = H_o(X + 2\pi/K_{\text{ext}})$  to represent linearly stable configurations. As detailed below, linearization about a spatially modulated base state generates an operator equation with spatially periodic coefficients. The resulting linear operator is no longer self-adjoint and the eigenvalues no longer purely real. Bloch decomposition provides an analytic tool well suited to this problem.

Bloch [35] demonstrated how to construct solutions—now called Bloch functions or Bloch waves—to linear evolution equations containing spatially periodic coefficients. He encountered this problem in the context of the Schrödinger equation for electron wave functions  $\Psi(\mathbf{r})$  subject to an atomic lattice representing a spatially periodic potential. He showed that the solutions can be described by the form  $\Psi(\mathbf{r}) = e^{i\mathbf{k}\cdot\mathbf{r}}u(\mathbf{r})$ , where the periodicity of the function  $u(\mathbf{r})$  is given by the periodicity of the underlying potential function. Since then, a similar approach has been used to solve various evolution equations with spatially periodic coefficients, including hydrodynamic problems involving pattern formation [32]. We therefore linearize Eq. (1) about the periodic base state  $H_o(X) = H_o(X + 2\pi/K_{\text{ext}})$  by expanding perturbations in terms of Bloch functions of wave number  $Q$ :

$$H(X, \tau) = H_o(X) + \sigma e^{\Omega(Q, K_{\text{ext}})\tau} H_Q(X) e^{iQX} \quad (46)$$

with  $H_Q(X) = H_o(X + 2\pi/Q)$ ,  $0 \leq Q \leq K_{\text{ext}}$ , and  $\sigma \ll 1$ . The range  $Q$  follows from observation that a Bloch function  $H_Q(X)$  can always be written in terms of another Bloch function  $e^{iMK_{\text{ext}}X} H_o(X)$  for integer values  $M$  and so wave numbers  $Q$  that fall outside the fundamental range can always be mapped back onto the fundamental range [32]. Substitution of Eq. (46) into Eq. (1) yields the corresponding eigenvalue equation:

$$\Omega H_Q = \mathcal{L}_Q\{H_Q\} = \left\{ \sum_{j=0}^4 a_j(X) \mathcal{D}_Q^j \right\} H_Q(X) \quad (47)$$

with  $\mathcal{D}_Q^j = \partial^j / \partial X^j + iQ$  and  $\mathcal{D}_Q^{j=0} = 1$ . For later analysis, we denote the eigenvalue with maximum real part as  $\Omega_{\text{max}}$  and its corresponding wave number  $Q_{\text{max}}$ .

As detailed next, the coefficients  $a_n$  depend nonlinearly on the functions  $H_o(X)$ , its higher-order derivatives, and the functions  $\Theta_H(X)^{(ij)}$ , which also depend nonlinearly on  $H_o(X)$ . It is therefore expected that perturbations to the spatially periodic base state  $H_o(X)$  will in general yield solutions  $H(X, \tau)$  not matching the periodicity of  $H_o(X)$ , thereby generating configurations not characterized by a

TABLE IV. Expressions for  $\Sigma(X)$  and  $\tilde{\Theta}(X)$  for case 1, 2 and 3 modulation.

	$\Sigma(X)$	$\tilde{\Theta}(X)$
Case 1	$D(X) = D_o[1 + \delta \cos(K_{\text{ext}}X)]$	1
Case 2	$\Theta_+(X) = 1 + \delta \cos(K_{\text{ext}}X)$	$1 + \delta \cos(K_{\text{ext}}X)$
Case 3	$\Theta_-(X) = \delta \cos(K_{\text{ext}}X)$	$1 - \delta \cos(K_{\text{ext}}X)$

single wave number  $K_{\text{ext}}$ . Such configurations will also be examined in more depth in Sec. VII.

The analytic expressions for the coefficient functions  $a_1, \dots, a_4$  are as follows, where superscripts indicated by a prime symbol denote differentiation with respect to  $X$ :

$$\begin{aligned} a_0 = & \mathcal{M}H_o'(\Sigma' \Theta_H^{(0,1)} + H_o' \Theta_H^{(1,0)}) \\ & + H_o[\mathcal{M}(\Sigma'' \Theta_H^{(0,1)} + \Sigma'^2 \Theta_H^{(0,2)} + H_o'' \Theta_H^{(1,0)}) \\ & + H_o'(-2H_o''' + 3\mathcal{M}\Sigma' \Theta_H^{(1,1)} + 2\mathcal{M}H_o'^2 \Theta_H^{(2,0)}) \\ & + \mathcal{M} \frac{H_o^2}{2} (\Sigma'' \Theta_H^{(1,1)} + \Sigma'^2 \Theta_H^{(1,2)} + H_o'' \Theta_H^{(2,0)} \\ & \quad + 2\Sigma' H_o' \Theta_H^{(2,1)} + H_o'^2 \Theta_H^{(3,0)}) \\ & - H_o^2 H_o'''' , \end{aligned} \quad (48a)$$

$$\begin{aligned} a_1 = & H_o \{ \mathcal{M}(\Sigma' \Theta_H^{(0,1)} + 2H_o' \Theta_H^{(1,0)}) \\ & + H_o[-H_o''' + \mathcal{M}(\Sigma' \Theta_H^{(1,1)} + H_o' \Theta_H^{(2,0)})] \} , \end{aligned} \quad (48b)$$

$$a_2 = \mathcal{M} \frac{H_o^2}{2} \Theta_H^{(1,0)} , \quad (48c)$$

$$a_3 = -H_o^2 H_o' , \quad (48d)$$

$$a_4 = -\frac{H_o^3}{3} . \quad (48e)$$

The expressions for the functions  $\Sigma(X)$  and  $\tilde{\Theta}(X)$  appearing above are listed in Table IV. The expressions for  $\Theta_H^{(i,0)}$  are given by

$$\Theta_H^{(1,0)} = \frac{-\kappa D \tilde{\Theta}(X)}{[D + (\kappa - 1)H_o(X)]^2} , \quad (49a)$$

$$\Theta_H^{(2,0)} = \frac{2(\kappa - 1)\kappa D \tilde{\Theta}(X)}{[D + (\kappa - 1)H_o(X)]^3} , \quad (49b)$$

$$\Theta_H^{(3,0)} = \frac{-6(\kappa - 1)^2 \kappa D \tilde{\Theta}(X)}{[D + (\kappa - 1)H_o(X)]^4} , \quad (49c)$$

where the expressions for  $\Theta_H^{(ij)}$  are listed in Table V. In Figs. 6–11(f) of Sec. VII, we draw direct comparison between the estimated growth rates  $\Omega$  given by Eq. (47) based on small perturbations to spatially periodic equilibrium states and results extracted from direct numerical simulations.



## VI. NUMERICAL MODEL AND PARAMETER CHOICES

Numerical solutions for  $H(X, \tau)$  for unmodulated and modulated systems governed by Eq. (1) are obtained by the method of lines. Spatial derivatives are discretized by fourth-order, centered finite differences and time stepping is based on backward differentiation. When ascertaining the influence of noise, simulations are initialized by interface functions describing a flat film with a small degree of surface roughness modeled by white Gaussian noise:

$$H(X_n, 0) = 1 + \mathcal{A}\mathcal{G}(X_n). \quad (50)$$

Here  $\mathcal{A} = 10^{-3}$  and  $\mathcal{G}(X_n)$  denotes random seed values drawn from a Gaussian distribution with standard deviation one. For initial states devoid of noise, the initial condition is simply set to the uniform value  $H(X, \tau = 0) = 1.0$ .

Those simulations initialized with noise free profiles, which included the bifurcation analysis in Sec. IV C and the Bloch wave and stability analysis in Sec. V, are carried out within a spatial domain of length  $L = 1$  containing  $N = 256$  grid points and representing one period of the modulation wave number  $K_{\text{ext}} = 2\pi$ . For those simulations with noisy initial conditions designed to mimic experimental conditions, the domain size is extended to  $L = 64$  with each subinterval  $L = 1$  containing  $N = 128$  grid points. For all simulations conducted, periodic boundary conditions are enforced by requiring  $H(X = -L/2, \tau) = H(X = +L/2, \tau)$ .

For all cases examined, the thermal conductivity ratio of air to liquid is set to a value  $\kappa = 0.25$  in line with experimental values [16–18,22]. The average boundary separation distance is also set to  $D_o = 5$  unless otherwise specified.

## A. Parameter range and resulting simplified relations

For the simulations in this work, the modulation wave number is held fixed at the value  $K_{\text{ext}} = 2\pi$  and sweeps of the ratio  $\mathcal{R} > 1$ , where

$$\mathcal{R} = \frac{K_{\text{ext}}}{K_c} = \frac{2\pi}{\sqrt{2} K_{\text{max}}}, \quad (51)$$

are carried out to elicit parameter ranges in modulated systems leading to periodic arrays with a smaller pitch than in corresponding unmodulated systems. As stated previously, the thermal conductivity ratio and average boundary separation distance are also held fixed at  $D_o = 5$  and  $\kappa = 0.25$ . The controlling dimensionless number  $\mathcal{M}$  in Eq. (1) then reduces to the approximate value

$$\mathcal{M} = \frac{8\pi^2 (D_o + \kappa - 1)^2}{3\mathcal{R}^2 \kappa D_o} \approx \frac{578}{15} \left( \frac{\pi}{\mathcal{R}} \right)^2, \quad (52)$$

indicating the scaling relation  $\mathcal{M} \sim \mathcal{R}^{-2}$ . Upon substitution of Eq. (51), the criterion given by Eq. (45) also reduces to the relation

$$\delta < \delta^*(\mathcal{R}) = \frac{4}{9\Upsilon} \sqrt{\frac{2}{c_3}} (\mathcal{R} - 1)^{3/2}, \quad (53)$$

where the values  $\Upsilon$  and  $c_3$  for case 1, 2 and 3 modulation are listed in Table II and Eq. (36), respectively. All relevant parameter values for the simulation results shown in Figs. 5 through 11 are provided in Table VI.

Identification of those normal modes that dominate fluid response during growth allowed determination of various physical mechanisms responsible for structure formation during different stages of the patterning process. To that end, spectral analysis was based on the norm  $\mathbb{N}(K/K_{\text{ext}}, \tau)$  of the discrete Fourier transform of the interface displacement according to

TABLE V. Functions  $\Theta_H^{(ij)}$  for case 1, 2 and 3 modulation.

$\Theta_H^{(ij)}$	Case 1	Case 2	Case 3
$\Theta_H^{(0,1)}$	$\frac{\kappa H_o(X)}{[D(X) + (\kappa - 1)H_o(X)]^2}$	$\frac{D_o - H_o(X)}{D_o + (\kappa - 1)H_o(X)}$	$\frac{\kappa H_o(X)}{D_o + (\kappa - 1)H_o(X)}$
$\Theta_H^{(0,2)}$	$\frac{-2\kappa H_o(X)}{[D(X) + (\kappa - 1)H_o(X)]^3}$	0	0
$\Theta_H^{(1,1)}$	$\frac{\kappa [D(X) + (1 - \kappa)H_o(X)]}{[D(X) + (\kappa - 1)H_o(X)]^3}$	$\frac{-\kappa D_o}{[D_o + (\kappa - 1)H_o(X)]^2}$	$\frac{\kappa D_o}{[D_o + (\kappa - 1)H_o(X)]^2}$
$\Theta_H^{(1,2)}$	$\frac{-2\kappa [D(X) + 2(1 - \kappa)H_o(X)]}{[D(X) + (\kappa - 1)H_o(X)]^4}$	0	0
$\Theta_H^{(2,1)}$	$\frac{2\kappa(1 - \kappa)[2D(X) + (1 - \kappa)H_o(X)]}{[D(X) + (\kappa - 1)H_o(X)]^4}$	$\frac{2\kappa(\kappa - 1)D_o}{[D_o + (\kappa - 1)H_o(X)]^3}$	$\frac{-2\kappa(\kappa - 1)D_o}{[D_o + (\kappa - 1)H_o(X)]^3}$

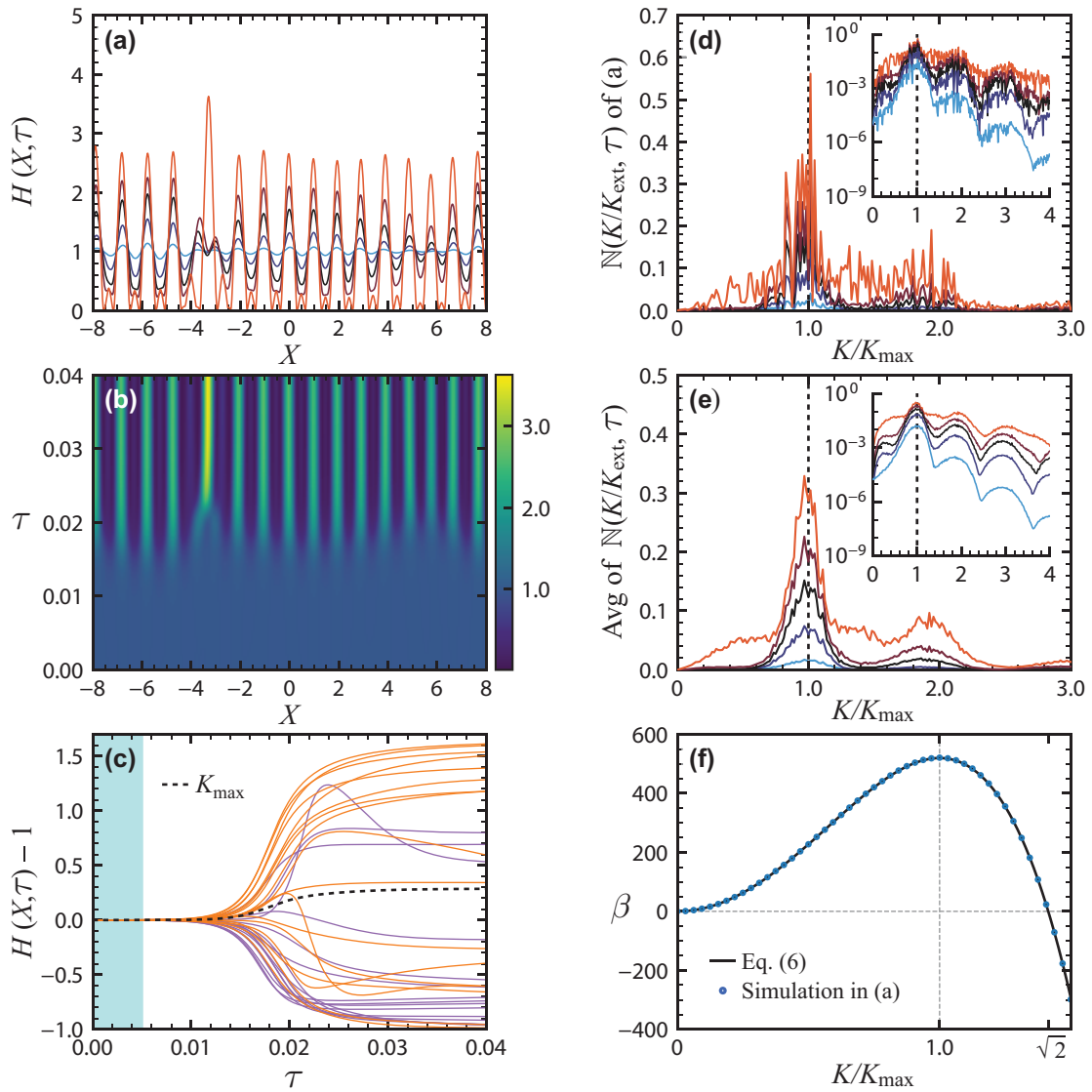


FIG. 5. Thermocapillary instability and growth of multiple protrusions for an unmodulated system ( $\delta = 0$ ) with a flat warmer boundary at  $Z = 0$  and a flat colder boundary at  $Z = 5.0$ . Parameter values given in Table VI along with selected times shown. (a) Evolution of  $H(X, \tau)$  for domain length  $-32 \leq X \leq +32$  (partial domain shown). (b) Plan view of structure formation in (a); color map denotes magnitude  $H(X, \tau)$ . (c) Time traces of  $H(X, \tau)$  at selected locations: dark curves (purple) signify values at  $X_i = -7.5, -6.5, \dots, +6.5, +7.5$ ; light curves (orange) signify values at  $X_i = -8.0, -7.0, -6.0, \dots, +6.0, +7.0, +8.0$ . (d) Results from Eq. (54) for the run in (a) with  $K_{\text{ext}}$  replaced by  $K_{\max}$ —inset shows same results on a log-linear scale. Vertical dashed line (black) denotes  $K_{\max}$  given by Eq. (9). (e) Averaged results from Eq. (54) based on 50 independent runs initialized by Eq. (50)—inset shows the same results on a log-linear scale. Curve  $K_{\max}$  in (c) represents the averaged values extracted from (e). (f) Modal growth rates  $\beta(K/K_{\max})$  from Eq. (6) for a noise-free initial condition and from Eq. (54) for 50 independent runs for  $0 \leq \tau \leq 0.005$  [shaded region in (c)]. Error bars from different runs are not visible since they are smaller than the marker diameter.

$$\begin{aligned} & \mathbb{N}(K/K_{\text{ext}}, \tau) \\ &= \left| \sum_{n=0}^{N-1} [H(X_n, \tau) - 1] e^{-2\pi i(n/N)(K/K_{\text{ext}})} \right|. \end{aligned} \quad (54)$$

For unmodulated systems,  $K_{\text{ext}}$  is replaced by  $K_{\max}$ . Equation (54) was evaluated for individual realizations

as well as averages based on 50 independent realizations seeded by different random numbers in the initial condition.

For cases involving continual growth without formation of an intermediate saturated periodic state, theoretical predictions from Eqs. (6) and (20) for the maximum exponential growth rates  $\beta(K/K_{\max})$  and  $\beta(K/K_{\text{ext}})$  based on a noise-free initial condition are directly compared to

TABLE VI. Parameter values for numerical solutions of case 1 and 2 modulation for films initialized by Eq. (50) with choices  $D_o = 5$ ,  $\kappa = 0.25$ , and  $K_{\text{ext}} = 2\pi$ . Resulting reduced expressions for  $\mathcal{R} = K_{\text{ext}}/K_c$  and  $\mathcal{M}$  are given by Eqs. (51) and (52), respectively. The variable  $\delta$  denotes the modulation amplitude value; times  $\tau_j$  signify the time stamps of configurations shown in Figs. 5 through 11.

	Case	$\mathcal{R}$	$\mathcal{M}$	$K_{\text{max}}/2\pi$	$K_{\text{ext}}/2\pi$	$Q_{\text{max}}/2\pi$	$\delta$	$\tau_j$
Figure 5	Unmodulated		760.618	1.0	0		0	0.013, 0.016, 0.018, 0.020, 0.040
Figure 6	1	1.2	264.103	0.589 26	1.0	0.5	0.10	0.050, 0.100, 0.115, 0.125, 0.140, 0.200
Figure 7	1	1.2	264.103	0.589 26	1.0		0.25	0.005, 0.010, 0.020, 0.050, 0.400
Figure 8	1	2.0	95.077	0.353 55	1.0	0.5	0.50	0.100, 0.300, 0.350, 0.400, 0.460
Figure 9	1	2.0	95.077	0.353 55	1.0		0.65	0.001, 0.002, 0.003, 0.004, 0.007
Figure 10	2	3.0	42.257	0.235 70	1.0	0.365	0.10	0.500, 1.500, 1.700, 1.800, 1.900, 2.500
Figure 11	2	3.0	42.257	0.235 70	1.0		0.40	0.001, 0.002, 0.004, 0.007, 0.020, 0.500

the modal growth rates extracted from Eq. (54) from runs initialized with the noisy initial condition in Eq. (50). The numerical values for the maximum modal growth rates are obtained from least-squares linear fits to the relation  $\ln \mathbb{N}(K/K_{\text{ext}}, \tau)$  versus  $\tau$  over the time interval specified.

For studies focused on the linear stability of Bloch periodic states, which tended to form at intermediate times, theoretical predictions for the maximum growth rates  $\Omega(Q, K/K_{\text{ext}})$  are computed from Eq. (47). The input base state functions  $H_o(X)$  for these computations corresponded to the late time (i.e.,  $\tau \rightarrow 1$ ) numerical solutions of Eq. (1) with  $L = 1$  and a noise-free initial condition  $H(X, \tau = 0) = 1.0$ . These results are directly compared to data extracted from Eq. (54) based on runs initialized by the noise condition in Eq. (50). For the parameter values used in this work, the maximum eigenvalues  $\Omega_{\text{max}}(Q, K_{\text{ext}})$  are always found to be real and positive, indicating that, when they form, Bloch states  $H_o(X)$  are linearly unstable to binary coalescence events. These events eventually lead to a final array pitch roughly twice as large as the Bloch wave pitch. The results and discussion presented below discuss our findings for case 1 and 2 systems. The results for case 3 systems exhibited similar trends and are not shown here.

Solutions for the various calculations described above are carried out using routines available in NumPy [36], an extensive PYTHON library for scientific computing. More information about these algorithms can be found elsewhere [37,38]. We note in passing that the assumptions underlying Eq. (1) require that no point of the moving interface can make contact with either the warmer or cooler boundary surface since physical effects that then ensue are not incorporated into this equation. In the numerical simulations, a stop condition is applied in order to prevent any interface contact with either solid boundary.

In the Supplementary Material provided [39], the interested reader will find animations of the numerical solutions presented in panels (a) and (d) of Figs. 5 through 11. These animations, which depict the solutions  $H(X, \tau)$  and  $\mathbb{N}(K/K_{\text{ext}}, \tau)$ , respectively, offer a more detailed view of

spatiotemporal wave interference effects and coalescence events that occur during pattern evolution.

## VII. RESULTS OF DIRECT NUMERICAL SIMULATIONS: REAL AND RECIPROCAL SPACE ANALYSIS

### A. Unmodulated system

The solutions  $H(X, \tau)$  in Fig. 5(a) depict onset and subsequent growth of the thermocapillary instability for an unmodulated system. Although the protrusion shapes and array pitch appear uniform at early times, the influence of white Gaussian noise in the initial condition coupled with binary coalescence events (e.g., near  $X = -4$ ) prevents formation of a periodic array. In particular, binary coalescence events produce taller structures that, according to the dynamics of thermocapillary flow, advance more rapidly toward the colder boundary than smaller neighboring protrusions. The colored image in Fig. 5(b) depicts a plan view of the evolving film thickness in (a). The resulting color gradients highlight the transition from a relatively uniform state at early time to a disordered state for  $\tau > 0.015$  exhibiting only short-range order.

Figure 5(c) depicts time traces of interface displacement for the run in (a). As evident, small amplitude growth gives way to rapid growth of ever taller protrusions and rapid thinning of interstitial regions between adjacent protrusions. Development of large viscous stresses within these ultrathin regions eventually constricts liquid flow and redistribution, thereby drastically slowing growth. The spread in the data at  $\tau = 0.4$  confirms a final state marked by significant variation in peak height, a situation which ultimately disfavors use of the thermocapillary instability as a patterning technique for large area arrays. The curve labeled  $K_{\text{max}}$ , which is extracted from Fig. 5(e) for the period in time indicated by the shaded region in (c), represents the evolution of the magnitude of the associated Fourier coefficient. As predicted, this most unstable mode from linear stability analysis dominates the pitch of the array formation process at early times. As time progresses, however, this periodicity is compromised by the influence of noise and coalescence events.

Shown in Fig. 5(d) are the results from Eq. (54) for the run in (a) with  $K_{\text{ext}}$  replaced by  $K_{\text{max}}$ . The observed broadband response reflects the influence of noisy initial conditions. The vertical dashed line represents the wave number  $K_{\text{max}}$  of the fundamental mode given by Eq. (9)—integer multiples of this value represent higher-order harmonics. The results in Fig. 5(e) represent the average spectral response based on 50 independent runs initialized by Eq. (50) with different seed values. The average response reveals more clearly the rapid growth of the  $K_{\text{max}}$  mode and its harmonics.

Shown in Fig. 5(f) is a comparison of the early time modal growth rates from Eq. (6) based on a noise-free initial condition with estimates of the run in (a) initialized by the white noise condition and extracted from (d) over the time interval  $0 \leq \tau \leq 0.005$ . The agreement is excellent, thereby establishing the dominance of the  $K_{\text{max}}$  mode at early times of the patterning process. However, the results in (b) and (c) are not encouraging since, while the protrusions at early and intermediate times are periodic, their peak heights are likely too small to be of use for micro-optical applications. Furthermore, while the structures attained at late times are significantly taller, they too are not useful since the configurations lack periodicity.

### B. Case 1: small amplitude modulation with

$$\mathcal{R} = K_{\text{ext}}/K_c = 1.2$$

It was shown in Secs. IV B and IV C that, for small amplitude modulation with wave number  $K_{\text{ext}}$  near  $K_c$ , there exists a maximum value of the modulation amplitude  $\delta^*$  given by Eq. (45) below which spatially periodic states are linearly stable to small disturbances and above which they are linearly unstable. In what follows, we demonstrate the different dynamics that ensue below and above  $\delta^*$  for case 1 modulation for parameter values  $\mathcal{R} = 1.2$  and  $\delta^* = 0.216349$ .

Shown in Fig. 6 are results for  $\delta = 0.10 < \delta^*$ . Figure 6(a) depicts the evolution of multiple protrusions advancing toward the colder sinusoidal boundary. The vertical dashed lines (blue) represent those points of the initial liquid film that are relatively cooler than adjacent regions due to their proximity to the overhangs of the cold boundary. After initial growth, several of the liquid protrusions undergo binary coalescence, producing taller structures whose tips on average no longer align with the dashed lines since the coalesced shapes can no longer sustain the pitch enforced by thermal modulation. Were the growth process solely controlled by thermocapillary forces without mitigation from capillary forces, then these tips would advance in alignment with the vertical lines. The fact that this does not occur reflects the inherent competition between thermocapillary and capillary forces, which varies in time. Figure 6(b) shows a plan view of the evolving film

thickness in (a). While, for  $\tau < 0.10$ , the array appears to be spatially periodic, uniformity is lost for  $\tau > 0.10$  whereupon numerous pairs of protrusions coalesce into single taller protrusions with corresponding faster growth than nearby formations. Such coalescence events lead to final state array configurations that are highly nonuniform and characterized by a larger average pitch than prescribed by the modulation wavelength.

Figure 6(c) depicts time traces of the run in (a). After initiation of film deformation, the system settles into a quasisteady periodic state dominated by the  $K_{\text{ext}}$  mode that persists for some time. The curves labeled  $K_{\text{max}}$  and  $Q_{\text{max}}$  (fastest growing mode from coalescence events) indicate corresponding results extracted from (e). This quasisteady configuration represents the resonantlike state given by Eq. (22). The formation of such a uniform, small amplitude periodic state suggests that modulated thermocapillary patterning of thin films offers a high-fidelity replication technique (provided the pattern can be solidified *in situ* during this stationary period). The results in Fig. 6(c) indicate that this state eventually becomes unstable to coalescence events in response to interactions induced by a noisy initial condition and interference of the  $K_{\text{ext}}$  and  $Q_{\text{max}}$  modes. Once the majority of peaks have coalesced into pairs, further growth is considerably restrained by the large viscous stresses that develop in the interstitial regions due to progressively more rapid thinning.

Shown in Fig. 6(d) are the values obtained from Eq. (54) for the run in (a). The average results in Fig. 6(e) more clearly highlight the broadband response with the development of significant peaks at  $Q_{\text{max}}$ ,  $K_{\text{ext}}$ , and its higher harmonics. These results, coupled with the modal curves shown in (c), indicate that while the spectral coefficient for  $K_{\text{ext}}$  remains strong over time, there develops a comparable contribution from  $Q_{\text{max}}$  as well. Film coarsening from coalescence, however, ultimately generates a final state marked by considerable nonuniformity in peak height and pitch.

Shown in Fig. 6(f) is a comparison of modal growth rates extracted from the spectral analysis for  $0.04 \leq \tau \leq 0.06$  along with the predictions for  $\Omega(Q, K_{\text{ext}})$  given by Eq. (47) for a noise-free steady periodic base state—see Sec. VII for a description of the input base state  $H_o(X)$ . In this run [as in those in Figs. 8(f) and 10(f) to be discussed later], the symmetry about  $\Omega/K_{\text{ext}} = 0.50$  reflects the periodicity of the underlying Bloch wave in Eq. (46) that must satisfy  $H_Q(X) = H_Q(X + 1)$ . The results confirm unstable growth for  $0 < Q/K_{\text{ext}} < 1.0$ , affirming the observed transition in (c) from a quasisteady periodic state to a nonuniform final state. The deviations between the eigenvalues  $\Omega(Q, K_{\text{ext}})$  and the spectral results underscore the influence of noisy initial conditions. These deviations, which increase significantly as  $Q$  approaches  $K_{\text{ext}}$ , evidence faster growth rates than estimated from a noise-free initial condition.



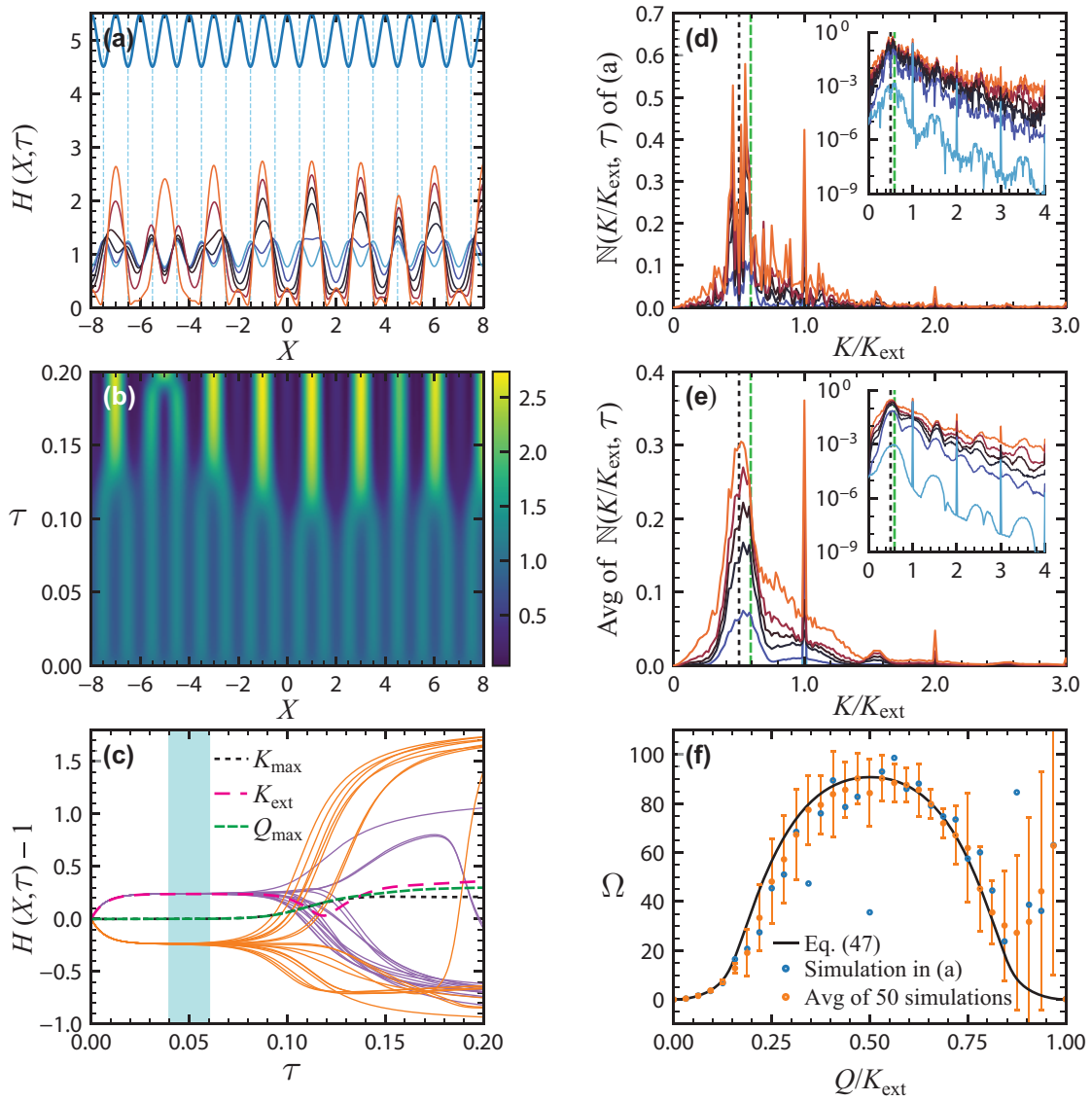


FIG. 6. Evolution dynamics for case 1 modulation with  $\mathcal{R} = 1.2$  and  $\delta = 0.10 < \delta^* = 0.216349$  for colder boundary position  $D(X) = 5.0[1 + \delta \cos(K_{\text{ext}}X)]$ , where  $K_{\text{ext}} = 2\pi$ . Additional parameter values listed in Table VI along with selected times shown. (a) Evolution of  $H(X, \tau)$  for  $-32 \leq X \leq 32$  (partial domain shown). (b) Plan view of structure formation in (a); color map denotes magnitude  $H(X, \tau)$ . (c) Time traces of  $H(X, \tau)$  at selected locations: dark curves (purple) signify values at  $X_i = -7.5, -6.5, \dots, +6.5, +7.5$ ; light curves (orange) signify values at  $X_i = -8.0, -7.0, -6.0, \dots, +6.0, +7.0, +8.0$ . (d) Results from Eq. (54) for the run in (a)—inset shows the same results on a log-linear scale. Vertical dashed lines signify values  $Q_{\text{max}}/K_{\text{ext}} = 0.5$  (dashed green) and  $K_{\text{max}}/K_{\text{ext}} = 0.58926$  (dashed black). (e) Averaged results from Eq. (54) based on 50 independent runs initialized by Eq. (50)—inset shows the same results on a log-linear scale. Curves  $K_{\text{max}}$ ,  $K_{\text{ext}}$ , and  $Q_{\text{max}}$  in (c) represent averaged values extracted from (e). (f) Modal growth rates  $\Omega(Q/K_{\text{ext}})$  from Eq. (47) for a noise-free periodic state and from Eq. (54) initialized by Eq. (50) for  $0.04 \leq \tau \leq 0.06$  [shaded region in (c)].

It has been previously reported that inclusion of stochastic thermal noise into the thin-film equation describing the competition between capillary and repulsive van der Waals forces tends to generate fluctuations in film thickness that accelerate dewetting [40]. While in our current work we imprint white noise into the initial condition for the film thickness (and not the thin-film equation nor the

boundary conditions), we too find that, under certain conditions, noise accelerates the transition from equilibrium periodic states at intermediate times to aperiodic states at late times resulting from coalescence of some adjacent protrusions. This behavior is especially pronounced near values  $Q \approx K_{\text{ext}}$  where resonant wavelength excitations likely promote such effects.

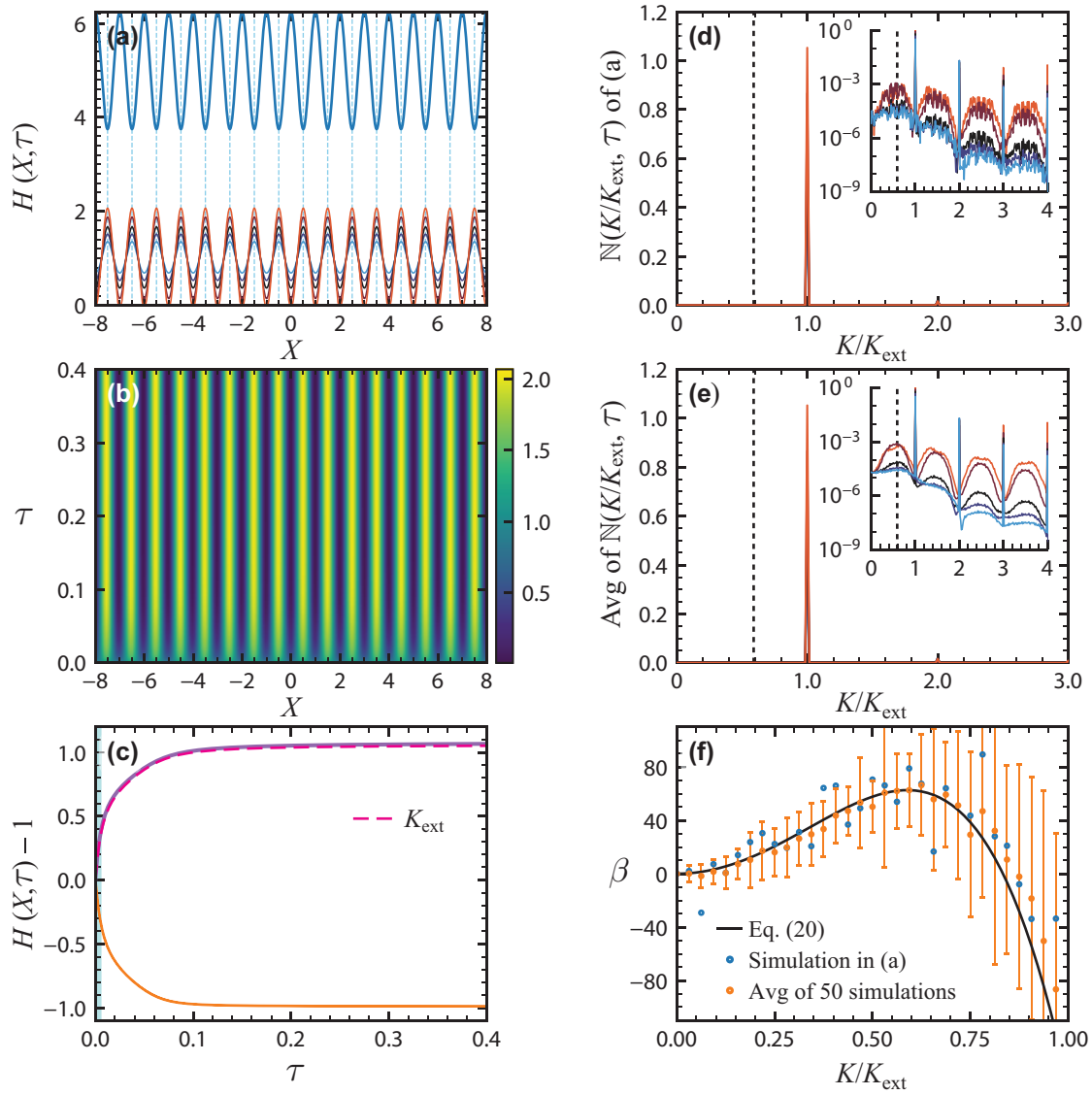


FIG. 7. Evolution dynamics for case 1 modulation with  $\mathcal{R} = 1.2$  and  $\delta = 0.25 > \delta^* = 0.216349$  for colder boundary position  $D(X) = 5.0[1 + \delta \cos(K_{\text{ext}}X)]$ , where  $K_{\text{ext}} = 2\pi$ . Additional parameter values listed in Table VI along with selected times shown. (a) Evolution of  $H(X, \tau)$  for  $-32 \leq X \leq 32$  (partial domain shown). (b) Plan view of structure formation in (a); color map denotes magnitude  $H(X, \tau)$ . (c) Time traces of  $H(X, \tau)$  at selected locations: dark curves (purple) signify values at  $X_i = -7.5, -6.5, \dots, +6.5, +7.5$ ; light curves (orange) signify values at  $X_i = -8.0, -7.0, -6.0, \dots, +6.0, +7.0, +8.0$ . (d) Results from Eq. (54) for the run in (a)—inset shows the same results on a log-linear scale. Vertical dashed line (black) denotes  $K_{\text{max}}$  given by Eq. (9). (e) Averaged results from Eq. (54) based on 50 independent runs initialized by Eq. (50)—inset shows the same results on a log-linear scale. Curve  $K_{\text{ext}}$  in (c) represents averaged values extracted from (e). (f) Modal growth rates  $\beta(K/K_{\text{ext}})$  from Eq. (20) for a noise-free initial condition and from Eq. (54) initialized by Eq. (50) for  $0 \leq \tau \leq 0.005$  [shaded region in (c)].

The behavior just described contrasts significantly with that for  $\delta = 0.25 > \delta^*$ . As evident in Fig. 7(a), here the profiles manifest rather perfect registration with the externally enforced pitch with strong uniformity in peak amplitude and shape for all times. The liquid tips advance in synchrony and align with the vertical dashed lines denoting the coldest points of the initial liquid film. The plan view in (b) highlights strong uniformity in growth with no evidence of coalescence despite the noisy initial

condition. The corresponding time traces in Fig. 7(c) neatly collapse onto two curves—the upper one showing peak heights and the lower one the valleys between peaks. The curve marked  $K_{\text{ext}}$  exactly follows the evolution of peak heights. The film patterning process rapidly approaches its asymptotic periodic configuration without formation of any intermediate, small amplitude periodic state nor subsequent coalesced state. Instead, the results in Figs. 7(d) and 7(e) confirm growth dominated by  $K_{\text{ext}}$

that is practically uninfluenced by noise, the effects of which only become visible in the inset image. This example shows that, for  $\delta > \delta^*$  and  $\mathcal{R}$  close to unity, thermal modulation is very effective in synchronizing rapid growth despite the presence of small amplitude noise in the initial condition.

The results in Fig. 7(f) contrast modal growth values from Eq. (20) for  $\beta(K/K_{\text{ext}})$  based on a noise-free initial condition with results extracted from the spectral analysis for  $0 \leq \tau \leq 0.005$  based on a noisy initial condition. The discrepancies in values increase with increasing  $K$  and become significantly larger as  $K \rightarrow K_{\text{ext}}$ . Capillary forces are therefore not as effective in suppressing thermocapillary growth in thin films subject to a small degree of noise. Once again, the influence of noise and resonant excitation effects near  $K_{\text{ext}}$  appears to increase instability growth rates.

### C. Case 1: larger amplitude modulation with $\mathcal{R} = K_{\text{ext}}/K_c = 2.0$

The analyses in Secs. IV B and IV C apply only to systems in which the external forcing ratio  $\mathcal{R}$  is close to unity and the modulation amplitude  $\delta$  much smaller than one. The numerical simulations described next were therefore conducted in order to explore modulation response beyond restrictions of the weakly nonlinear analysis.

Shown in Fig. 8 are results for simulations conducted with  $\mathcal{R} = 2.0$  and  $\delta = 0.50$ . The evolution in (a) is similar to that discussed Fig. 6(a)—both depict multiple protrusions advancing toward the colder sinusoidal boundary. After initial growth, the majority of protrusions undergo binary coalescence, producing taller structures whose tips on average no longer align with the dashed lines since the coalesced shapes can no longer sustain the pitch enforced by the modulation. In this example, the final peak heights are smaller than in Fig. 6(a) because the surface force ratio  $\mathcal{M}$  is about 2.8 times smaller in value—see Table VI. The thermocapillary stresses promoting growth are therefore relatively weaker. The plan view in (b) reveals the formation of a quasisteady periodic state that persists for a prolonged period of time before eventually giving way to the instability causing coalescence events.

The time traces in Fig. 8(c) highlight the rapid onset and persistence of a quasisteady periodic state, which closely tracks the spectral coefficient of the  $K_{\text{ext}}$  mode. There is no significant contribution from mode  $K_{\text{max}}$ . This quasisteady configuration represents the resonantlike state given by Eq. (22). Eventually, the appearance and growth of the unstable mode  $Q_{\text{max}}$ , which causes coalescence of adjacent protrusions, dominates the  $K_{\text{ext}}$  mode, which undergoes progressive decay. This behavior is also evident from the results in (d), which show the dominance of  $K_{\text{ext}}$  at early and intermediate times and that of  $Q_{\text{max}}$  at late times. By contrast, the small contribution from  $K_{\text{max}}$  at very early

times decays away rapidly. The averaged spectral response in (e) highlight this exchange in modal response even more clearly.

Shown in Fig. 8(f) is a comparison of modal growth rates from the spectral analysis for  $0.05 \leq \tau \leq 0.10$  with the values  $\Omega(Q, K_{\text{ext}})$  from Eq. (47) for a noise-free steady periodic base state. [See the description near the end of Sec. VIA justifying the choice of periodic input base states  $H_o(X)$ .] The results confirm unstable growth for  $0 < Q/K_{\text{ext}} < 1.0$ , affirming the observed transition in (c) from a quasisteady periodic state to a nonuniform final state. The deviations between the eigenvalues  $\Omega(Q, K_{\text{ext}})$  and the spectral results underscore the influence of noisy initial conditions. For wave numbers  $Q/K_{\text{ext}} < 0.50$ , the agreement is excellent, while for  $Q/K_{\text{ext}} > 0.50$ , the disagreement becomes substantial. As noted earlier, the combined influence of noise and resonant excitation effects near  $K_{\text{ext}}$  appears to accelerate the instability growth rate of the intermediate periodic state. Despite the fact that the given choice for  $\mathcal{R}$  and  $\delta$  generate a fairly wide spread in data for  $0.50 < Q/K_{\text{ext}} < 0.75$ , the mean values are in fairly good agreement with Eq. (47). From a practical point of view, these results confirm that the regular array patterns representative of the long-lived periodic state must be affixed in place before onset of the instability leading to coalescence.

The results in Fig. 9 reflect the dynamical behavior for even larger modulation amplitude  $\delta = 0.65$ . The images in Figs. 9(a)–9(c) evidence extremely rapid formation of highly uniform periodic arrays over a time window that is 2 orders of magnitude smaller than in previous examples. This is mostly due to the fact that the liquid protrusions here can only advance a small distance before contacting the overhangs of the cooler boundary surface. The time traces in Fig. 9(c) neatly collapse onto two curves—the upper one representing peak heights and the lower one the valleys between peaks. Although the  $K_{\text{ext}}$  mode closely tracks the evolution in peak heights, the discrepancy between the two growth rates increases in time. This is likely due to increased interference from growth of the harmonic  $K/K_{\text{ext}} = 2.0$ , which is evident in (d). This observation is based on the comparison with the results in Figs. 7(c) and 7(d), where there is no contribution from higher harmonics of  $K_{\text{ext}}$  and consequently excellent agreement between the time traces of the peaks and the growth of the spectral coefficient of the fundamental mode  $K_{\text{ext}}$ . Despite this slight mismatch with the pitch set by the fundamental mode, it appears that the thermal modulation is nonetheless able to corral fluid response into strong registration with the spatial forcing despite a noisy initial condition.

The results in Fig. 9(f) contrast modal growth values from Eq. (20) for  $\beta(K/K_{\text{ext}})$  based on a noise-free initial condition with results from spectral analysis for  $0 \leq \tau \leq 0.0004$  based on a noisy initial condition. The values

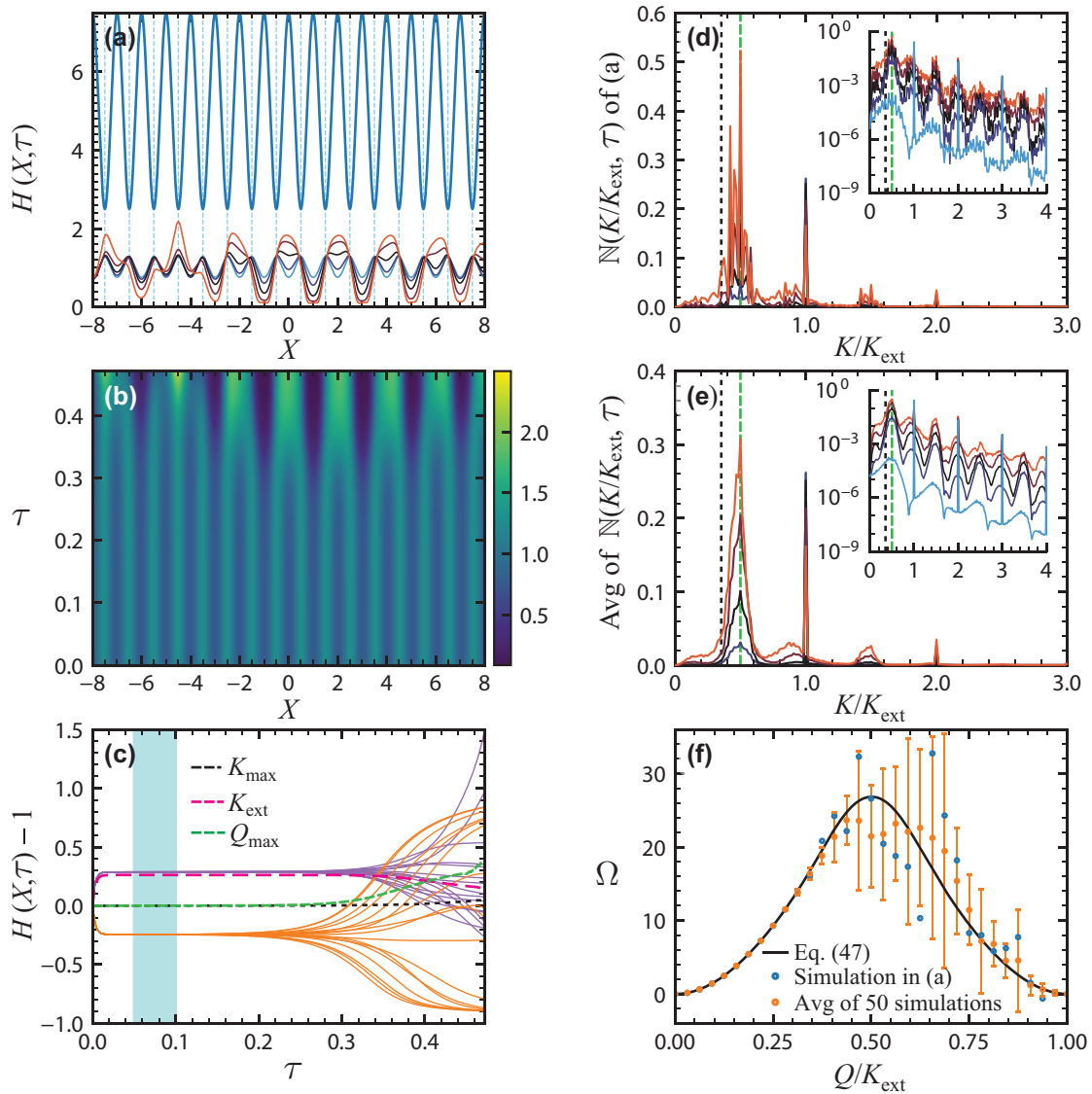


FIG. 8. Evolution dynamics for case 1 modulation with  $\mathcal{R} = 2.0$  and  $\delta = 0.50$  for colder boundary position  $D(X) = 5.0[1 + \delta \cos(K_{\text{ext}}X)]$ , where  $K_{\text{ext}} = 2\pi$ . Additional parameter values listed in Table VI along with selected times shown. (a) Evolution of  $H(X, \tau)$  for  $-32 \leq X \leq +32$  (partial domain shown). (b) Plan view of structure formation in (a); color map denotes magnitude  $H(X, \tau)$ . (c) Time traces of  $H(X, \tau)$  at selected locations: dark curves (purple) signify values at  $X_i = -7.5, -6.5, \dots, +6.5, +7.5$ ; light curves (orange) signify values at  $X_i = -8.0, -7.0, -6.0, \dots, +6.0, +7.0, +8.0$ . (d) Results from Eq. (54) for the run in (a)—inset shows the same results on a log-linear scale. Vertical dashed lines signify the values  $K_{\text{max}}/K_{\text{ext}} = 0.35355$  (black) and  $Q_{\text{max}}/K_{\text{ext}} = 0.5$  (green). (e) Averaged results from Eq. (54) based on 50 independent runs initialized by Eq. (50)—inset shows the same results on a log-linear scale. Curves  $K_{\text{max}}$ ,  $K_{\text{ext}}$ , and  $Q_{\text{max}}$  in (c) represent averaged values extracted from (e). (f) Modal growth rates  $\Omega(Q/K_{\text{ext}})$  from Eq. (47) for a noise-free periodic state and from Eq. (54) initialized by Eq. (50) for  $0.05 \leq \tau \leq 0.10$  [shaded region in (c)].

of  $\beta(K/K_{\text{ext}})$  are positive over the range  $0 < K/K_{\text{ext}} < 0.50$ , with a maximum near  $(K/K_{\text{ext}} = 0.3593750, \beta = 8.1084752)$ . There is substantial discrepancy between the simulation results and Eq. (20), which increases significantly as  $Q$  approaches  $K_{\text{ext}}$ . The results suggest that the presence of white noise, likely enhanced by resonant excitations near  $K_{\text{ext}}$ , triggers amplification of modes that would otherwise decay in time due to capillary leveling.

#### D. Case 2: small to large amplitude modulation with $\mathcal{R} = K_{\text{ext}}/K_c = 3.0$

As depicted in Fig. 2, modulation of the thermal field can also be enforced with flat and parallel boundaries by maintaining a spatially periodic temperature distribution along the hotter or colder substrate. We discuss next a couple of examples for case 2 modulation with  $\Theta_+ = 1 + \delta \cos(K_{\text{ext}}X)$ . As before, we seek guidelines on imprinting films with a finer pitch than accessible to unmodulated



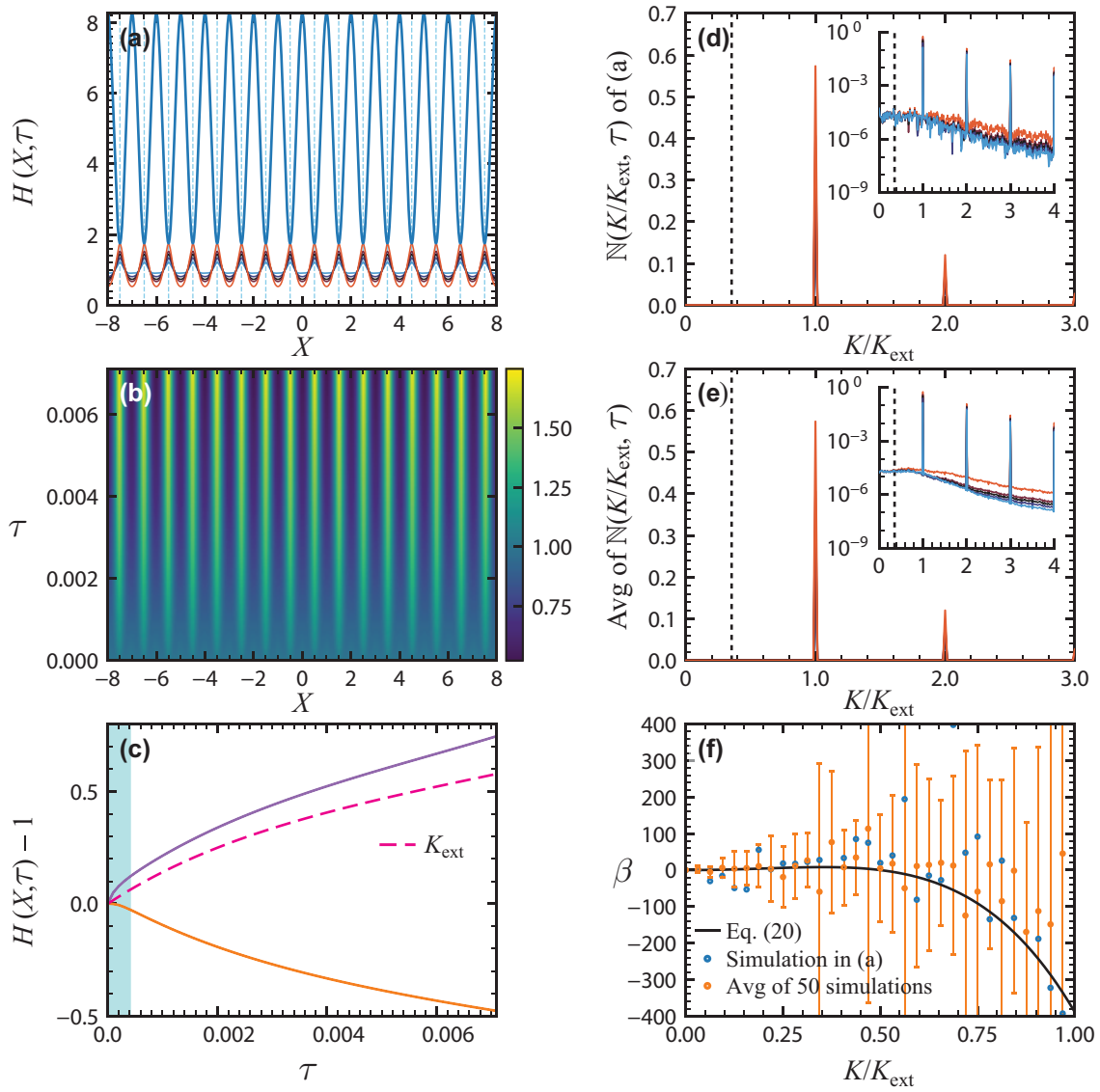


FIG. 9. Evolution dynamics for case 1 modulation with  $\mathcal{R} = 2.0$  and  $\delta = 0.65$  for colder boundary position  $D(X) = 5.0[1 + \delta \cos(K_{\text{ext}}X)]$ , where  $K_{\text{ext}} = 2\pi$ . Additional parameter values listed in Table VI along with selected times shown. (a) Evolution of  $H(X, \tau)$  for  $-32 \leq X \leq +32$  (partial domain shown). (b) Plan view of structure formation in (a); color map denotes magnitude  $H(X, \tau)$ . (c) Time traces of  $H(X, \tau)$  at selected locations: dark curves (purple) signify values at  $X_i = -7.5, -6.5, \dots, +6.5, +7.5$ ; light curves (orange) signify values at  $X_i = -8.0, -7.0, -6.0, \dots, +6.0, +7.0, +8.0$ . (d) Results from Eq. (54) for the run in (a)—inset shows the same results on a log-linear scale. Vertical dashed line (black) denotes  $K_{\text{max}}$  given by Eq. (9). (e) Averaged results from Eq. (54) based on 50 independent runs initialized by Eq. (50)—inset shows the same results on a log-linear scale. Curve  $K_{\text{ext}}$  in (c) represents averaged values extracted from (e). (f) Modal growth rates  $\beta(K/K_{\text{ext}})$  from Eq. (20) for a noise-free initial condition and from Eq. (54) initialized by Eq. (50) for  $0 \leq \tau \leq 0.0004$  [shaded region in (c)].

systems and here examine systems with  $\mathcal{R} = K_{\text{ext}}/K_c = 3.0$  and  $\delta = 0.10, 0.40$ . While the smaller value of  $\delta$  falls in line with the assumptions of the weakly nonlinear analysis presented in Sec. IV B, the ratio  $\mathcal{R}$  is too far from unity for those predictions to hold.

Shown in Fig. 10 are results of simulations conducted with  $\mathcal{R} = 3.0$  and  $\delta = 0.10$ . The colored horizontal strip shown at the bottom of the image in (a) depicts the periodic

thermal modulation of the warmer substrate—the darkest segments (red) and corresponding vertical dashed lines signify the hottest points of the substrate. At early times, the liquid film, now in direct contact with the modulated boundary, undergoes rapid thinning in the vicinity of the hottest points due to the thermocapillary effect, which draws fluid away from the warmer and toward the cooler regions. As time progresses, the majority of protrusions

undergo coalescence to form fewer and taller peaks. The final configuration resembles a highly irregular array with significant nonuniformity in peak height, shape, and pitch. The plan view in (b) and time traces in (c) illustrate more clearly the immediate formation of a quasisteady periodic state dominated by mode  $K_{\text{ext}}$  that persists for a prolonged period in time. The evolution time scales in this example are about an order of magnitude larger than those in Figs. 6 and 7 since here  $\mathcal{M}$  is about a factor 6.25 smaller—see Table VI. The time traces and wave number curves in Fig. 10(c) confirm that the intermediate time periodic state and spectral coefficient of the  $K_{\text{ext}}$  mode track closely together in time. Eventually, the growth of the unstable mode  $Q_{\text{max}}$  overcomes influence from the  $K_{\text{ext}}$  mode that undergoes continual decay. This behavior is also evident from the results in (d), which show the dominance of  $K_{\text{ext}}$  at early and intermediate times and that of  $Q_{\text{max}}$  at late times. The small contribution from  $K_{\text{max}}$  at very early times quickly decays away. The averaged spectral response in (e) highlight this exchange in modal response even more clearly.

The results in Fig. 10(f) show the modal growth rates  $\Omega(Q/K_{\text{ext}})$  from Eq. (47) for a noise-free periodic state along with spectral results for  $0.20 \leq \tau \leq 0.40$  initialized by the noisy condition in Eq. (50). The growth rates are everywhere positive over the entire range  $0 < Q/K_{\text{ext}} < 1.0$ , indicating that the quasisteady periodic state is unstable to coalescence events. Surprisingly, despite the presence of white noise, the agreement between the results of the spectral analysis and Eq. (47) is remarkably good and likely due to two reasons. The first is that the liquid film is in direct contact with the thermally modulated boundary, which affords more direct external control. In addition, the ratio  $\mathcal{R}$  is fairly large so as to suppress any effects from underlying resonant excitations that occur for smaller values of that ratio.

The behavior shown in Fig. 11 for  $\delta = 0.40$  contrasts sharply with that in Fig. 10 for smaller modulation amplitude. Despite the fact that the ratio  $\mathcal{M} = 42.257$  is much smaller than in all the other examples shown in Figs. 5–9, the fluid undergoes rapid formation of highly uniform arrays with larger amplitude that are in excellent registry with the externally prescribed pitch. The plan view in (b) highlights the persistence of the array regularity, which, as evident in Fig. 11(c), is controlled by the modulation wave number  $K_{\text{ext}}$ . The results in Figs. 11(d) and 11(e) indicate dominance of the  $K_{\text{ext}}$  mode with hardly any influence from its higher harmonics and no indication of mode  $K_{\text{max}}$ . This example confirms that thermal modulation enforced by direct contact of the film with the modulated boundary allows superior control over the pitch and shape of the final periodic state.

The results in Fig. 11(f) contrast the modal growth rates for  $\beta(K/K_{\text{ext}})$  from Eq. (20) for a noise-free initial condition with results from spectral analysis for  $0 \leq$

$\tau \leq 0.005$  based on a noisy initial condition. The values  $\beta(K/K_{\text{ext}})$  are positive over the range  $0 < K/K_{\text{ext}} < 0.328\,125$ , with a maximum near the point  $(K/K_{\text{ext}} = 0.234\,375, \beta = 1.603\,239\,6)$ . The mean value from the spectral analysis is in excellent agreement with the theoretical estimate predicated on a noise-free initial condition. These results indicate that the large value of  $\mathcal{R} = 3.0$  prevents any resonant excitation effects from setting in and allows capillary forces to dampen growth rates at larger wave numbers, just as occurs in the idealized analysis with noise-free initial conditions.

### E. Correlation between critical modulation amplitude $\delta_{\text{num}}^*$ and $\mathcal{R}$

In Sec. IV C, we derived the expression for Eq. (45) [later simplified to Eq. (53)] for the critical modulation amplitude  $\delta^*(\mathcal{R})$ . Those expressions are only valid in the limit of small amplitude corrugations for which  $\mathcal{R} \rightarrow 1$  from above. Below this critical value, the film adopts an equilibrium periodic shape dominated by  $K_{\text{ext}}$  that can persist for some time but is ultimately unstable to coalescence events. Above this value, the film immediately locks into  $K_{\text{ext}}$  and undergoes accelerated growth until contact with one of the boundary substrates occurs. Here we present results of numerical simulations for cases 1, 2 and 3 initialized by a noise-free initial condition  $H(X, \tau = 0) = 1.0$  and restricted to a single period domain of length  $L = 1$ . This restriction allowed numerical computation of the correlation  $\delta_{\text{num}}^*(\mathcal{R})$  based on ideal film shapes, i.e., shapes not subject to noise-induced interference or coalescence. The results are extracted from a bisection search of the modulation amplitude at fixed value  $\mathcal{R}$ —unlike the analysis leading to Eq. (45), these results are not limited to small values of amplitude modulation. In this study, the simulations are terminated when any point of the interface thins to a value  $H = 0.01$ . By such time, evolution has slowed substantially and film states manifest the saturated shapes shown.

Shown in Fig. 12(a) is an example for case 1 modulation with  $D_o = 5$  for  $\mathcal{R} = 1.2$ . The critical modulation amplitude is found to equal  $\delta_{\text{num}}^* = 0.2016$ , slightly below the estimate 0.2163 from Eq. (45). Below this value, the asymptotic configurations  $H(X, \tau \rightarrow 1)$  assume interface shapes situated well away from either solid boundary. By contrast, values  $\delta > 0.2016$  generate asymptotic shapes with a relatively flat depleted central region. Shown in Fig. 12(b) are the numerical results  $\delta_{\text{num}}^*$  for the system in (a) for values  $\mathcal{R}$  ranging from 1.0 to 4.0 along with estimates predicted by Eq. (53). The excellent agreement evident in the inset image as  $\mathcal{R} \rightarrow 1$  confirms the validity of the theoretical analysis.

Shown in Fig. 12(c) are results for  $\delta_{\text{num}}^*$  obtained for four examples of boundary thermal modulation and two values

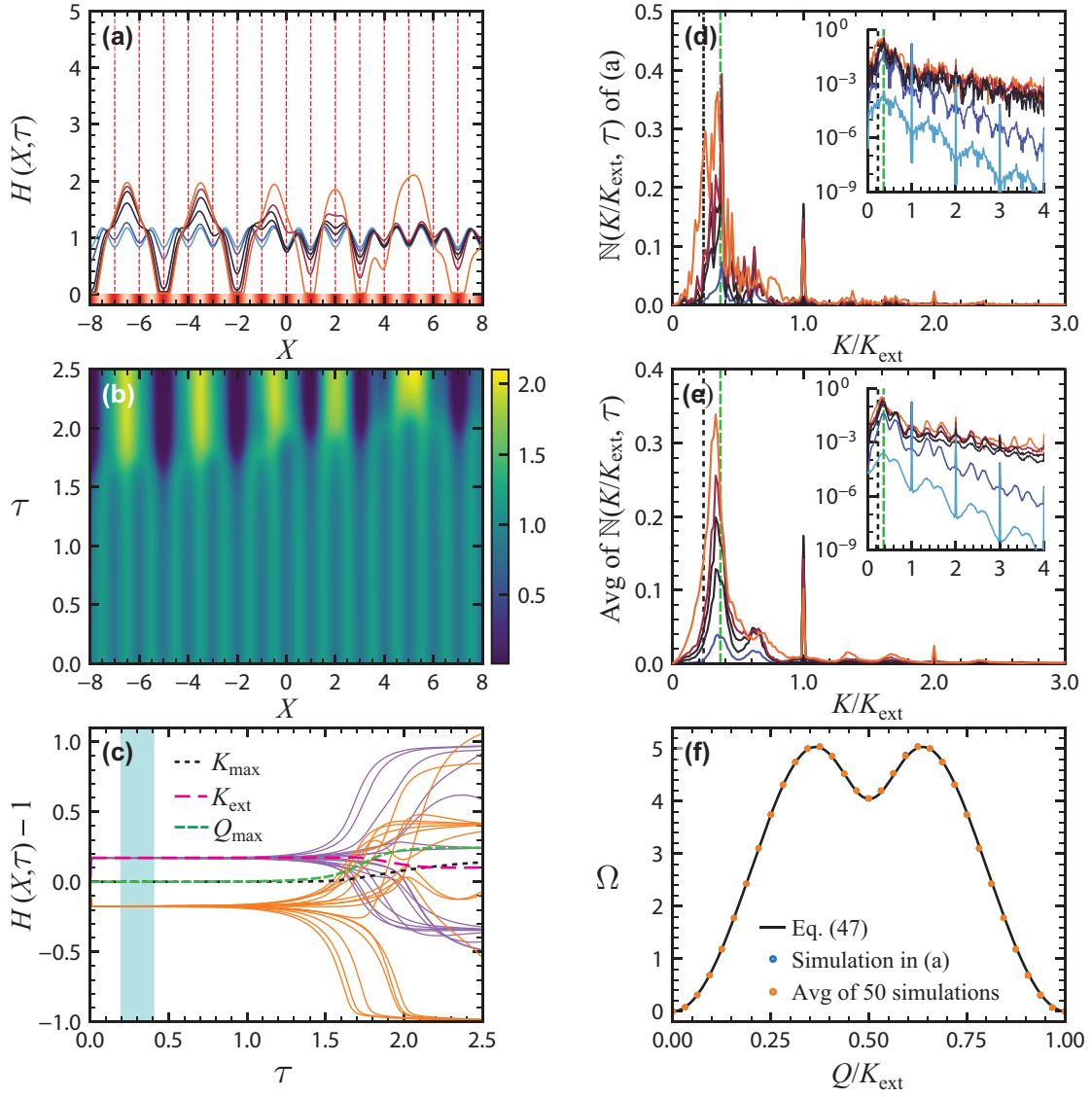


FIG. 10. Evolution dynamics for case 2 modulation with  $\mathcal{R} = 3.0$  and  $\delta = 0.10$  for thermal modulation of warmer boundary temperature  $\Theta_+ = 1 + \delta \cos(K_{\text{ext}}X)$ , where  $K_{\text{ext}} = 2\pi$ . Additional parameter values listed in Table VI along with selected times shown. (a) Evolution of  $H(X, \tau_j)$  for  $-32 \leq X \leq +32$  (partial domain shown). (b) Plan view of structure formation in (a); color map denotes magnitude  $H(X, \tau)$ . (c) Time traces of  $H(X, \tau)$  at selected locations: dark curves (purple) signify values at  $X_i = -7.5, -6.5, \dots, +6.5, +7.5$ ; light curves (orange) signify values at  $X_i = -8.0, -7.0, -6.0, \dots, +6.0, +7.0, +8.0$ . (d) Results from Eq. (54) for the run in (a)—inset shows the same results on a log-linear scale. Vertical dashed lines signify  $K_{\text{max}}/K_{\text{ext}} = 0.23570$  (black) and  $Q_{\text{max}}/K_{\text{ext}} = 0.365$  (green). (e) Averaged results from Eq. (54) based on 50 independent runs initialized by Eq. (50)—inset shows the same results on a log-linear scale. Curves  $K_{\text{max}}$ ,  $K_{\text{ext}}$ , and  $Q_{\text{max}}$  in (c) represent averaged values extracted from (e). (f) Modal growth rates  $\Omega(Q/K_{\text{ext}})$  from Eq. (47) for a noise-free periodic state and from Eq. (54) initialized by Eq. (50) for  $0.20 \leq \tau \leq 0.40$  [shaded region in (c)]. Error bars from multiple simulations are not visible since they are smaller than the marker diameter.

of average boundary separation distance  $D_o$ . These include case 1, 2, and 3 cosine modulation (see Fig. 2), and a case 1 system with a square well modulation. The results indicate that, for larger values of  $D_o$ , case 2 systems for  $\mathcal{R} \lesssim 3.5$  require much smaller values of the modulation amplitude to produce final states with large aspect ratios. Smaller values of  $D_o$  follow this trend only for small values of  $\mathcal{R}$ . For increasing values of  $\mathcal{R}$ , however, case 1 systems with square well modulation are favored instead.

## VIII. SUMMARY AND CONCLUDING REMARKS

The thin-film systems examined in this work are based on thermocapillary flow in which regions of a liquid layer that are slightly thicker than neighboring regions experience faster growth than lower-lying regions. In unmodulated systems, analysis and simulations based on an intrinsic long-wavelength instability predict growth of a periodic array of protrusions that continually advance toward a

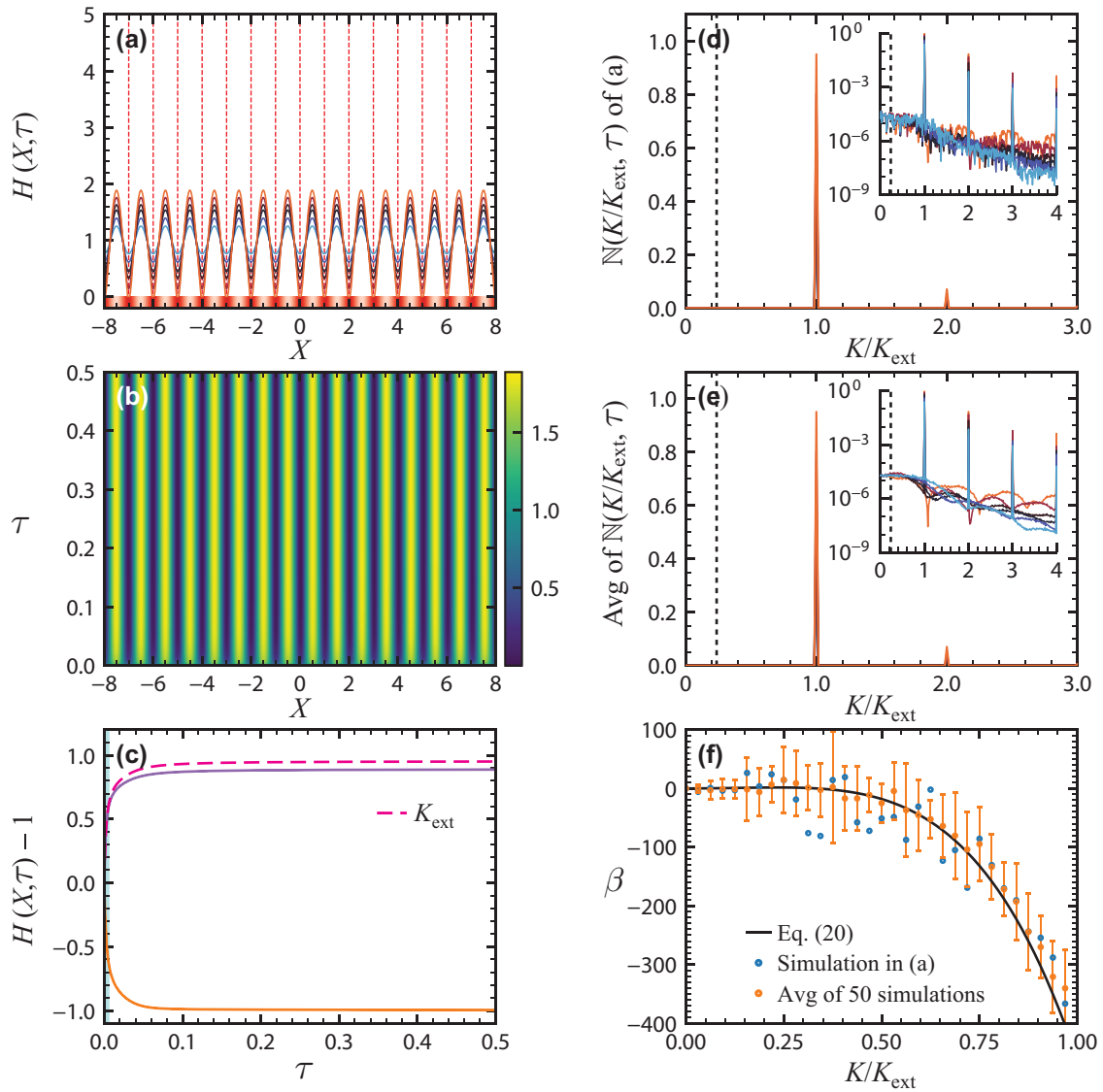


FIG. 11. Evolution dynamics for case 2 modulation with  $\mathcal{R} = 3.0$  and  $\delta = 0.40$  for thermal modulation of warmer boundary temperature  $\Theta_+ = 1 + \delta \cos(K_{\text{ext}}X)$ , where  $K_{\text{ext}} = 2\pi$ . Additional parameter values listed in Table VI along with selected times shown. (a) Evolution of  $H(X, \tau_j)$  for  $-32 \leq X \leq 32$  (partial domain shown). (b) Plan view of structure formation in (a); color map denotes magnitude  $H(X, \tau)$ . (c) Time traces of  $H(X, \tau)$  at selected locations: dark curves (purple) signify values at  $X_i = -7.5, -6.5, \dots, +6.5, +7.5$ ; light curves (orange) signify values at  $X_i = -8.0, -7.0, -6.0, \dots, +6.0, +7.0, +8.0$ . (d) Results from Eq. (54) for the run in (a)—inset shows the same results on a log-linear scale. Vertical dashed line denotes  $K_{\text{max}}/K_{\text{ext}} = 0.23570$  (black). (e) Averaged results from Eq. (54) based on 50 independent runs initialized by Eq. (50)—inset shows the same results on a log-linear scale. Curve  $K_{\text{ext}}$  in (c) represents averaged values extracted from (e). (f) Modal growth rates  $\beta(K/K_{\text{ext}})$  from Eq. (20) for a noise-free initial condition and from Eq. (54) initialized by Eq. (50) for  $0 \leq \tau \leq 0.005$  [shaded region in (c)].

cooler substrate with a fixed pitch set by the most unstable wavelength. However, even a very small degree of noise, which in this study is imprinted onto the initial condition for the film profile, causes highly asynchronous and disordered growth with short-range order at best. Since noise is ubiquitous, we conclude that sole reliance on this intrinsic instability as a lithographic method for generating uniform microarray patterns is unlikely ever to succeed.

It is shown, however, that even in the presence of noisy initial conditions, augmentation of the flow process

by spatially periodic boundary thermal modulation can successfully induce synchronous growth of highly uniform protrusion arrays. For comparable parameter values, these arrays not only form much more rapidly but can be designed to have a finer pitch than accessible to unmodulated systems. A comprehensive study of the spatiotemporal dynamics in modulated systems reveals how the thermal modulation amplitude and spatial frequency induce resonant wavelength excitations that sustain wave locking with the modulation field.



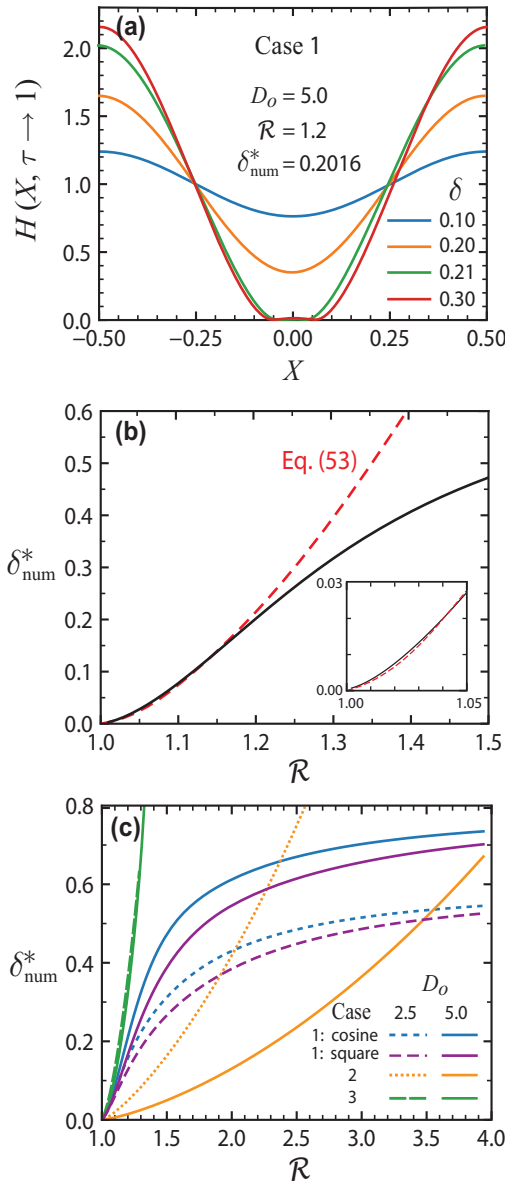


FIG. 12. Influence of boundary modulation amplitude and wave-number ratio  $\mathcal{R}$  on saturated film shapes as  $\tau \rightarrow 1$ . (a) Saturated film shapes for increasing values  $\delta_{\text{num}}^*$  for a case 1 system with  $D_o = 5$  and  $\mathcal{R} = 1.2$ . (b) Results for  $\delta_{\text{num}}^*(\mathcal{R})$  for the system in (a) plotted alongside estimates from Eq. (53). (c) Results for  $\delta_{\text{num}}^*(\mathcal{R})$  for four examples of boundary thermal modulation and two values of the average boundary separation distance  $D_o$ .

For given ratios  $\mathcal{R} = K_{\text{ext}}/K_c > 1$ , we show that there exists a critical value of the modulation amplitude that distinguishes between two types of saturated periodic states. Below the critical value, a flat film with very small surface roughness modeled by white noise evolves at intermediate times into a highly uniform array with small amplitude periodic protrusions and a pitch that closely matches the prescribed pitch  $2\pi/K_{\text{ext}}$ . The supporting analysis and numerical simulations reveal that these saturated states can persist for long periods of time. During this extended

period, such arrays can be solidified *in situ* by electronic means to yield extended films ideally suited to microlens applications. Eventually, these states destabilize and transition to nonuniform configurations characterized by irregular coalescence of some adjacent protrusions. The coalescence process ultimately causes significant nonuniformity in element shape and an average local pitch larger than prescribed by modulation. Fabrication of highly uniform arrays requires only that the evolution process be terminated sometime prior to onset of any coalescence event.

Above the critical modulation amplitude, a flat film with very small amplitude surface roughness modeled by white noise undergoes immediate wave locking with the modulation spatial frequency to generate highly synchronous growth with pitch  $2\pi/K_{\text{ext}}$ . In this case, the system does not settle into any intermediate small amplitude state; instead, the periodic protrusions advance very rapidly and in perfect unison toward the cooler substrate until contact is achieved, if so desired. For some parameter values, the peak heights can become so large that further growth is only stymied by the constraint of constant volume. In this case, fluid redistribution from the thin warmer regions to the thicker cooler regions of the film then significantly slows due to development of large frictional forces (i.e., viscous stresses) in the interstitial segments. In this regime, fabrication of highly uniform arrays can be terminated electronically at any time during the evolution process, depending on the aspect ratio desired.

These findings offer a compelling solution to the current dilemma of lithographic patterning of thin films based solely on pattern generation from an intrinsic instability. Despite the highly nonlinear character of the governing evolution equation, implementation of spatially periodic thermal modulation allows resonant wavelength excitations to synchronize rapid growth of an array even in the presence of noise. The process leads to highly uniform microarrays with an even finer pitch than in comparable unmodulated systems. We anticipate that the approach outlined in this work will resolve similar challenges currently encountered with other lithographic techniques that rely on hydrodynamic instabilities in ultrathin films.

## ACKNOWLEDGMENTS

Y.H.C. gratefully acknowledges financial support from a 2021–22 Croucher Foundation Graduate Scholarship. S.M.T. wishes to thank Dr. Nan Liu for useful discussions during early stages of this project. The authors also wish to thank Dr. Peter Thompson for assistance with computing resources used in this study.

[1] H. P. Herzig, ed., *Micro-Optics: Elements, Systems and Applications* (Taylor & Francis, Bristol, PA, 1997).

- [2] J. Jahns and K.-H. Brenner, *Microoptics: From Technology to Applications*, Springer Series in Optical Sciences (Springer-Verlag, New York, NY, 2004).
- [3] R. Grunwald, *Thin Film Micro-Optics: New Frontiers of Spatio-Temporal Beam Shaping* (Elsevier B. V., Amsterdam, The Netherlands, 2007).
- [4] H. Zappe, *Fundamentals of Micro-Optics* (Cambridge University Press, New York, 2010).
- [5] A. A. Darhuber and S. M. Troian, Principles of microfluidic actuation by modulation of surface stresses, *Annu. Rev. Fluid Mech.* **37**, 425 (2005).
- [6] A. del Campo and E. Arzt, Fabrication approaches for generating complex micro- and nanopatterns on polymeric surfaces, *Chem. Rev.* **108**, 911 (2008).
- [7] O. K. C. Tsui and T. P. Russell, eds., *Polymer Thin Films*, Soft Condensed Matter, Vol. 1 (World Scientific, Hackensack, NJ, 2008).
- [8] J. Rodríguez-Hernández and C. E. Drummond, eds., *Polymer Surfaces in Motion – Unconventional Patterning Methods* (Springer International Publishing, Switzerland, 2015).
- [9] E. Schäffer, Ph.D. thesis, Konstanz University, 2001.
- [10] E. Schäffer, S. Harkema, R. Blossey, and U. Steiner, Temperature gradient induced instability in polymer films, *Europhys. Lett.* **60**, 255 (2002).
- [11] E. Schäffer, S. Harkema, M. Roerdink, R. Blossey, and U. Steiner, Morphological instability of a confined polymer film in a thermal gradient, *Macromol.* **36**, 1645 (2003).
- [12] E. Schäffer, S. Harkema, M. Roerdink, R. Blossey, and U. Steiner, Thermomechanical lithography: Pattern replication using a temperature gradient driven instability, *Adv. Mater.* **15**, 514 (2003).
- [13] M. Dietzel and S. M. Troian, Formation of Nanopillar Arrays in Ultrathin Viscous Films: The Critical Role of Thermocapillary Stresses, *Phys. Rev. Lett.* **103**, 074501 (2009).
- [14] M. Dietzel and S. M. Troian, Thermocapillary patterning of nanoscale polymer films, *MRS Proc.* **1179**, BB08 (2009).
- [15] M. Dietzel and S. M. Troian, Mechanism for spontaneous growth of nanopillar arrays in ultrathin films subject to a thermal gradient, *J. Appl. Phys.* **108**, 074308 (2010).
- [16] E. McLeod, Y. Liu, and S. M. Troian, Experimental Verification of the Formation Mechanism for Pillar Arrays in Nanofilms Subject to Large Thermal Gradients, *Phys. Rev. Lett.* **106**, 175501 (2011).
- [17] K. R. Fiedler and S. M. Troian, Early time instability in nanofilms exposed to a large transverse thermal gradient: Improved image and thermal analysis, *J. Appl. Phys.* **120**, 205303 (2016).
- [18] K. R. Fiedler and S. M. Troian, Differential colorimetry measurements of fluctuation growth in nanofilms exposed to large surface thermal gradients, *J. Appl. Phys.* **125**, 065303 (2019).
- [19] C. Zhou and S. M. Troian, Self-similar cuspidal formation by runaway thermocapillary forces in thin liquid films, *New J. Phys.* **21**, 013018 (2019).
- [20] T. G. Albertson and S. M. Troian, Electrified cone formation in perfectly conducting viscous liquids: Self-similar growth irrespective of Reynolds number, *Phys. Fluids* **31**, 102103 (2019).
- [21] C. Zhou and S. M. Troian, Multiplicity of Inertial Self-Similar Conic Shapes in an Electrified Liquid Metal, *Phys. Rev. Appl.* **15**, 044001 (2021).
- [22] E. McLeod and S. M. Troian, in *Laser Applications to Photonic Applications*, CLEO 2011 - OSA Tech. Digest (Optical Society of America, 2011).
- [23] R. E. Kelly and D. Pal, Thermal convection with spatially periodic boundary conditions: Resonant wavelength excitation, *J. Fluid Mech.* **86**, 433 (1978).
- [24] A. Manor, R. Hagberg, and E. Meron, Wave-number locking in spatially forced pattern-forming systems, *Europhys. Lett.* **83**, 10005 (2008).
- [25] A. Manor, R. Hagberg, and E. Meron, Wave number locking and pattern formation in spatially forced systems, *New J. Phys.* **11**, 063016 (2009).
- [26] G. Seiden, S. Weiss, J. H. McCoy, W. Pesch, and E. Bodenschatz, Pattern Forming System in the Presence of Different Symmetry-Breaking Mechanisms, *Phys. Rev. Lett.* **101**, 214503 (2008).
- [27] D. Feldman, R. Nagao, T. Bansagi, I. R. Epstein, and M. Dolnik, Turing patterns in the chlorine dioxide-iodine-malonic acid reaction with square spatial periodic forcing, *Phys. Chem. Chem. Phys.* **14**, 6577 (2012).
- [28] A. M. Higgins and R. A. L. Jones, Anisotropic spinodal dewetting as a route to self-assembly of patterned surfaces, *Nature* **404**, 476 (2000).
- [29] V. S. Mitlin, Dewetting of solid surface: Analogy with spinodal decomposition, *J. Colloid Interface Sci.* **156**, 491 (1993).
- [30] J. C.-T. Kao, A. A. Golovin, and S. H. Davis, Rupture of thin films with resonant substrate patterning, *J. Colloid Interface Sci.* **303**, 532 (2006).
- [31] A. Oron, S. H. Davis, and S. G. Bankoff, Long-scale evolution of thin liquid films, *Rev. Mod. Phys.* **69**, 931 (1997).
- [32] M. Cross and H. Greenside, *Pattern Formation and Dynamics in Nonequilibrium Systems* (Cambridge University Press, New York, 2009).
- [33] When the temperatures of two flat boundaries are reversed such that the liquid film is supported on a cooler substrate, then  $\Delta T_c < 0$  and therefore  $\mathcal{M} < 0$ . For such systems, both terms on the right-hand side of Eq. (6) are negative and so the liquid film is always linearly stable, irrespective of the value of  $K$ .
- [34] C. M. Bender and S. A. Orzag, *Advanced Mathematical Methods for Scientists and Engineers* (McGraw Hill Book Company, New York, NY, 1978).
- [35] F. Bloch, Über die quantenmechanik der electronen im kristallgittern, *Z. Phys.* **52**, 555 (1928).
- [36] NumPy V1.22, NumPy Developers, <http://www.numpy.org/>.
- [37] T. E. Oliphant, *Guide to NumPy*, edited by K. Watson (Continuum Press, Continuum Analytics, Inc., 2015), 2nd ed.
- [38] P. Virtanen, *et al.*, SciPy 1.0: Fundamental algorithms for scientific computing in Python, *Nat. Methods* **17**, 261 (2020).
- [39] See Supplementary Material at <http://link.aps.org/supplemental/10.1103/PhysRevApplied.18.064090> for animations of numerical solutions  $H(X, \tau)$  and their discrete Fourier transforms, corresponding to the data in panels (a) and (d) of Figs. 5 through 11.
- [40] G. Grün, K. Mecke, and M. Rauscher, Thin film flow influenced by thermal noise, *J. Stat. Phys.* **56**, 1261 (2006).